

Jupiter’s low-altitude auroral zones: Fields, particles, plasma waves, and density depletions

Sulaiman Ali H.¹, Allegrini Frederic², Clark George³, Gladstone Randy², Kotsiaros Stavros⁴, Kurth William S¹, Mauk Barry H.⁵, Szalay Jamey R.⁶, Bagenal Fran⁷, Bonfond Bertrand⁸, Connerney John E. P.⁴, Ebert Robert Wilkes², Elliott Sadie Suzanne⁹, Gershman Daniel J⁴, Hospodarsky George Blair¹, Hue Vincent¹⁰, Lysak Robert L.⁹, Masters Adam¹¹, Santolik Ondrej¹², Saur Joachim¹³, and Bolton Scott J²

¹University of Iowa

²Southwest Research Institute

³Johns Hopkins University Applied Physics Laboratory

⁴NASA Goddard Space Flight Center

⁵Johns Hopkins University

⁶Princeton University

⁷University of Colorado Boulder

⁸Université de Liège

⁹University of Minnesota

¹⁰SWRI

¹¹Imperial College London

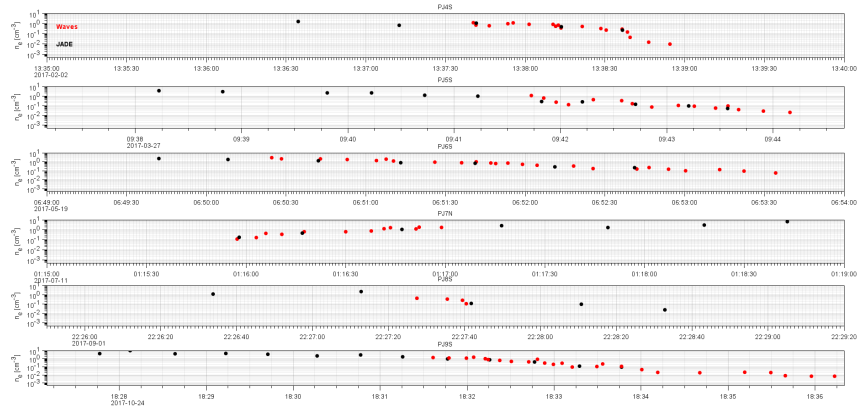
¹²Department of Space Physics, Institute of Atmospheric Physics of the Czech Academy of Sciences

¹³University of Cologne

November 16, 2022

Abstract

The Juno spacecraft’s polar orbits have enabled direct sampling of Jupiter’s low-altitude auroral field lines. While various datasets have identified unique features over Jupiter’s main aurora, they are yet to be analyzed altogether to determine how they can be reconciled and fit into the bigger picture of Jupiter’s auroral generation mechanisms. Jupiter’s main aurora has been classified into distinct “zones”, based on repeatable signatures found in energetic electron and proton spectra. We combine fields, particles, and plasma wave datasets to analyze Zone-I and Zone-II, which are suggested to carry the upward and downward field-aligned currents, respectively. We find Zone-I to have well-defined boundaries across all datasets. H⁺ and/or H₃⁺ cyclotron waves are commonly observed in Zone-I in the presence of energetic upward H⁺ beams and downward energetic electron beams. Zone-II, on the other hand, does not have a clear poleward boundary with the polar cap, and its signatures are more sporadic. Large-amplitude solitary waves, which are reminiscent of those ubiquitous in Earth’s downward current region, are a key feature of Zone-II. Alfvénic fluctuations are most prominent in the diffuse aurora and are repeatedly found to diminish in Zone-I and Zone-II, likely due to dissipation, at higher altitudes, to energize auroral electrons. Finally, we identify sharp and well-defined electron density depletions, by up to two orders of magnitude, in Zone-I, and discuss their important implications for the development of parallel potentials, Alfvénic dissipation, and radio wave generation.



1 **Jupiter’s low-altitude auroral zones: Fields, particles,** 2 **plasma waves, and density depletions**

3 A. H. Sulaiman,¹ F. Allegrini,^{2,3} G. Clark,⁴ G. R. Gladstone,^{2,3} S. Kotsiaros,⁵ W. S. Kurth,¹ B. H.
4 Mauk,⁴ J. R. Szalay,⁶ F. Bagenal,⁷ B. Bonfond,⁸ J. E. P. Connerney,^{9,10} R. W. Ebert,^{2,3} S. S.
5 Elliott,¹¹ D. J. Gershman,¹⁰ G. B. Hospodarsky,¹ V. Hue,² R. L. Lysak,¹¹ A. Masters,¹² O.
6 Santolík,^{13,14} J. Saur,¹⁵ S. J. Bolton¹

7 Corresponding author: A.H. Sulaiman, Department of Physics and Astronomy, University of
8 Iowa, Iowa City, Iowa, USA. (ali-sulaiman@uiowa.edu)

9 ¹Department of Physics and Astronomy, University of Iowa, Iowa City, IA, USA.

²Southwest Research Institute, San Antonio, TX, USA.

³Department of Physics and Astronomy, University of Texas at San Antonio, San Antonio, TX, USA.

⁴Johns Hopkins University, Applied Physics Laboratory, Laurel, MD, USA.

⁵DTU-Space, Technical University of Denmark, Kongens Lyngby, Denmark

⁶Department of Astrophysical Sciences, Princeton University, Princeton, NJ, USA

⁷Laboratory for Atmospheric and Space Physics, University of Colorado Boulder, Boulder, CO, USA.

⁸Space Sciences, Technologies and Astrophysics Research Institute, LPAP, Université de Liège, Liège, Belgium

⁹Space Research Corporation, Annapolis, MD, USA

¹⁰NASA/Goddard Space Flight Center, Greenbelt, Maryland, USA.

¹¹Minnetota Institute for Astrophysics, School of Physics and Astronomy, University of Minnesota, Minneapolis, MN, USA.

¹²Blackett Laboratory, Imperial College London, London, UK.

¹³Department of Space Physics, Institute of Atmospheric Physics of the Czech Academy of Sciences, Prague, Czechia.

¹⁴Faculty of Mathematics and Physics, Charles University, Prague, Czechia.

¹⁵Institute of Geophysics and Meteorology, University of Cologne, Cologne, Germany

- 10 • We discuss how the various fields, particles, and plasma wave phenomena of Jupiter’s
11 low-altitude auroral zones are related
12 • We confirm that Zone-I and Zone-II are Jupiter’s upward and downward field-aligned
13 current regions
14 • We identify large-scale electron density depletions over the aurora zones and discuss the
15 implications for auroral acceleration processes

16 **Abstract**

17 The Juno spacecraft's polar orbits have enabled direct sampling of Jupiter's low-altitude auroral
18 field lines. While various datasets have identified unique features over Jupiter's main aurora, they
19 are yet to be analyzed altogether to determine how they can be reconciled and fit into the bigger
20 picture of Jupiter's auroral generation mechanisms. Jupiter's main aurora has been classified into
21 distinct "zones", based on repeatable signatures found in energetic electron and proton spectra. We
22 combine fields, particles, and plasma wave datasets to analyze Zone-I and Zone-II, which are
23 suggested to carry the upward and downward field-aligned currents, respectively. We find Zone-I
24 to have well-defined boundaries across all datasets. H^+ and/or H_3^+ cyclotron waves are commonly
25 observed in Zone-I in the presence of energetic upward H^+ beams and downward energetic electron
26 beams. Zone-II, on the other hand, does not have a clear poleward boundary with the polar cap,
27 and its signatures are more sporadic. Large-amplitude solitary waves, which are reminiscent of
28 those ubiquitous in Earth's downward current region, are a key feature of Zone-II. Alfvénic
29 fluctuations are most prominent in the diffuse aurora and are repeatedly found to diminish in Zone-
30 I and Zone-II, likely due to dissipation, at higher altitudes, to energize auroral electrons. Finally,
31 we identify sharp and well-defined electron density depletions, by up to two orders of magnitude,
32 in Zone-I, and discuss their important implications for the development of parallel potentials,
33 Alfvénic dissipation, and radio wave generation.

34

35

36

37

38

39

40

41

42

43

44

45

46

1. Introduction

47 The combination of Jupiter's strong magnetic field, rapid rotation, and internally sourced mass
48 loading creates a magnetosphere that is fundamentally different from its terrestrial counterpart.
49 Structurally, the magnetosphere is inflated with the average observed distance of the magnetopause
50 far greater than the expected distance predicted from the internal dipolar magnetic pressure
51 standing off the external solar wind dynamic pressure (Joy et al. 2002). Mass loading of iogenic
52 plasma in the magnetosphere at a widely assumed rate of ~ 1 ton/s, primarily in the form of S and
53 O (in various charge states), greatly enhances the internal pressure owing to centrifugal, thermal,
54 and magnetic stresses, thereby pushing the magnetopause farther out. The action of these forces
55 confines the heavy plasma into the equatorial region of Jupiter's magnetosphere as a thin current
56 sheet, with varying thickness as a function of local time imposed by Jupiter's rotation (Khurana et
57 al., 2004; Thomas et al., 2004).

58 Dynamically, conservation of angular momentum breaks down the corotation of iogenic plasma
59 as it is transported radially outward. This introduces a significant azimuthal component to Jupiter's
60 magnetic field, starting in the middle magnetosphere ($\gtrsim 10 R_J$; $1 R_J = 71,492$ km as Jupiter's
61 equatorial radius). This large-scale configuration has been thought to be the framework for
62 Jupiter's main auroral oval as a current system imparts the required $\mathbf{J} \times \mathbf{B}$ force to enforce
63 corotation (Hill, 1979; Cowley & Bunce, 2001; Kivelson & Southwood, 2005). Charge density
64 continuity is satisfied by field-aligned currents and this is the basis upon which magnetosphere-
65 ionosphere coupling is established. This steady-state picture has been modelled extensively to
66 explain the observed brightness and location of Jupiter's main auroral oval (e.g. Nichols and
67 Cowley, 2004; Ray et al., 2010) by citing a relationship between parallel potentials and field-
68 aligned currents, originally developed for Earth's aurora (Knight, 1973). A consequence of this is
69 a mono-energetic or peaked electron distribution as current-carrying electrons unidirectionally
70 gain energy, $q\phi_{\parallel}$, proportional to the potential drop. A different approach put forth by Saur et al.
71 (2002, 2003) emphasizes the importance of prevalent small-scale magnetic perturbations brought
72 about by radial transport in Jupiter's magnetosphere. The authors hypothesized that Jupiter's
73 magnetosphere-ionosphere coupling is inherently time-dependent and mediated by weak
74 magnetohydrodynamic turbulence, whereby Alfvén waves nonlinearly interact with one another
75 as they partially reflect off density gradients. As these fluctuations undergo a turbulent cascade
76 toward kinetic scales, wave dissipation takes place and stochastically accelerates electrons. The
77 commonly observed broadband, bidirectional electron distributions in the low altitude regions of
78 Jupiter's aurora have brought to the fore the importance of the time-dependent nature of Jupiter's
79 magnetosphere (e.g. Mauk et al., 2017a; 2017b; Allegrini et al., 2017; Saur et al., 2018; Lysak et
80 al., 2021).

81 Prior to Juno's arrival, Jupiter's main aurora was investigated using remote observations and was
82 found to be more powerful and less variable than Earth's aurora (e.g. Waite et al., 2001; Gladstone
83 et al., 2002; Grodent et al., 2015). The principal difference is that Jupiter's aurora is primarily
84 driven by the internal dynamics of its magnetosphere, whereas Earth's is primarily driven by the
85 external solar wind (Cowley & Bunce, 2001; Hill, 2001). Recent modelling shows that most of the
86 polar cap region is threaded by magnetic flux that closes within the planet while only a small
87 crescent-shaped region of flux is 'open' to the solar wind (Zhang et al., 2021). This is attributed to
88 slow reconnection rates at the magnetopause relative to the timescale of planetary rotation, thereby

89 limiting the amount of magnetic flux that can be open (McComas and Bagenal, 2007; Delamere
90 and Bagenal, 2010; Masters, 2017; 2018).

91 The Juno spacecraft's low-perijove, polar orbits have enabled *in-situ* sampling of low-altitude
92 magnetic field lines threading Jupiter's polar aurora (e.g., Allegrini et al., 2017; Kurth et al., 2017a;
93 Mauk et al., 2017c). Juno's instruments have made direct measurements of critical observables
94 connected to the main aurora, namely the characteristics of precipitating electrons (e.g., Allergini
95 et al., 2020a; Mauk et al., 2020), magnetic field perturbations (Kotsiaros et al., 2019; Gershman et
96 al., 2019), radio and plasma wave emissions (e.g., Kurth et al., 2017a; 2018; Louarn et al., 2017),
97 as well as high-resolution ultraviolet (e.g., Bonfond et al., 2017; Gladstone et al., 2017) and
98 infrared (e.g., Mura et al., 2017) imagery. Altogether, these afford the capability to examine the
99 seemingly unique macro- and micro-physics sustaining Jupiter's aurora.

100 A key finding related to Jupiter's auroral particles is the often-observed broadband energetic field-
101 aligned electrons with a power law extending into the MeV range and a lack of sharp peak in
102 energy (Mauk et al., 2017a; 2017b; 2018). These electron beams can have energy fluxes exceeding
103 3 W/m^2 and exhibit bidirectionality that is more often asymmetric, with a systematically preferred
104 direction depending on latitude (Mauk et al., 2020). This appears to be the dominant precipitating
105 electron signature associated with the brightest aurora at Jupiter (Allegrini et al., 2020a; Mauk et
106 al., 2017b) and is in contrast with Earth's brightest aurora where they have been demonstrated to
107 be powered by inverted V distributions set up by parallel potentials (Carlson et al., 1998; Ergun et
108 al., 1998). The more familiar peaked energy distributions in the form of inverted-V electron and
109 ion distributions have also been observed by Juno, indicating that large-scale parallel electric
110 potentials also play a role (Clark et al., 2017; 2018). Although these two phenomena are disparate
111 in nature, they are believed to be closely associated with one another and have both been identified
112 to operate together in a single auroral zone as defined by Mauk et al. (2020) and summarized
113 below.

114 Using the JEDI instrument (described in the next section) with orbits favoring the duskside, Mauk
115 et al. (2020) classified Jupiter's main aurora into three distinct zones, two of which will be the
116 focus of this work. These are Zone-I and Zone-II, comprising regions of the aurora dominated by
117 persistent and repeatable signatures of field-aligned energetic electrons.

- 118 1. Zone-I (ZI): At the intermediate latitudes of the main auroral oval, this is characterized by
119 more intense electron populations within the downward loss cone than outside, and with
120 greater downward electron intensities and energy fluxes than upward.
- 121 2. Zone-II (ZII): At the higher latitudes, this is characterized by more intense electron
122 populations within the upward loss cone than outside, and with greater or equal upward
123 electron intensities and energy fluxes than downward. Here, remarkably, the downward
124 fluxes are nevertheless still sufficient to cause observable and powerful auroral intensities.

125 Zone-I and Zone-II have been suggested to be associated with upward and downward electric
126 currents, respectively, for a single event (Mauk et al., 2020). Equatorward of these zones is the
127 diffuse aurora (Dif-A), characterized with more intense high-energy electron populations outside
128 of the loss cone than within, and with greater downward electron intensities and energy fluxes than
129 upward.

130 Poleward of the zones is the polar cap – a vast and dynamic region where persistent highly field-
 131 aligned, upgoing energetic electrons have been observed (both inverted-V and broadband
 132 distributions, albeit spatially separated) simultaneously with upgoing broadband emissions
 133 interpreted as the whistler mode (Ebert et al., 2017; Elliott et al., 2018a; 2018b; Mauk et al., 2020;
 134 Paranicas et al., 2018). There has been ongoing research on plasma processes in this region and
 135 this will not be the focus of this study (e.g. Elliott et al., 2020; Shi et al., 2020; Masters et al.,
 136 2021).

137 In this paper, we combine all four instruments (described in the next section) from Juno’s fields
 138 and particles package to reconcile the various repeatable features exhibited by particle spectra,
 139 electric and magnetic field spectra, as well as field-aligned currents across Jupiter’s auroral zones.

140 **2. Instruments and Data Description**

141 We utilize four *in-situ* instruments onboard Juno with fields- and particles-measuring capabilities.

142 The Waves instrument measures an electric field component, E_y , using a 4.8 m tip-to-tip electric
 143 dipole antenna that is parallel to the spacecraft y -axis (Kurth et al., 2017). Its containment within
 144 the spin (x - y) plane means two electric field components are effectively measured twice per spin
 145 with a period of 30 seconds. A magnetic search coil measures a magnetic field component, B_z ,
 146 using a single sensor mounted along the spacecraft’s spin (z) axis. We utilize Waves data provided
 147 by the Low Frequency Receiver which covers the frequency ranges of 50 Hz – 20 kHz
 148 simultaneously for the E- and B-fields at 50 kilosamples per second. This frequency range is
 149 sufficient to capture plasma waves well below and above and the proton cyclotron frequency, f_{cH^+} ,
 150 in the near-Jupiter environment, by virtue of the very high magnetic field strength.

151 This Waves suite provides the capability to distinguish between electrostatic, $\delta E(f) \gg c\delta B(f)$, and
 152 electromagnetic, $\delta E(f) \sim c\delta B(f)$, waves below 20 kHz. Furthermore, the Poynting vector direction
 153 at a given frequency, $\delta \vec{E}(f) \times \delta \vec{B}(f) / \mu_0$, can be resolved, although incomplete measurement of
 154 all three E- and three B-field components means some assumptions are necessary. We mitigate
 155 this issue by reasonably assuming that the plasma waves are propagating either almost parallel or
 156 anti-parallel to \vec{B}_0 . Only one component of the Poynting vector can be resolved, which is along the
 157 spacecraft x -axis and its sign is compared with the sign of the background magnetic field’s x -
 158 component, B_{0x} . The sign of the Poynting vector component is determined from the mutual phases
 159 between E_y and B_z , with the mutual phases $\phi_{E_y-B_z}$ and coherency, $C_{E_y-B_z}$ calculated. In the northern
 160 hemisphere, the combination of $\phi_{E_y-B_z} \approx 0^\circ$ (180°) and a positive B_{0x} indicates upgoing
 161 (downgoing) plasma waves, i.e., away from (toward) Jupiter. The reverse is true when either B_{0x}
 162 is negative or the spacecraft is in the southern hemisphere. This technique has been used at Jupiter
 163 to constrain the directionality of lightning-induced rapid whistlers (Kolmašová et al., 2018),
 164 plasma waves in Jupiter’s aurora (Kurth et al., 2018), as well as Io’s Main Alfvén Wing (Sulaiman
 165 et al., 2020).

166 The Jupiter Energetic-particle Detector Instrument (JEDI) measures energetic charged particle
 167 distributions. For this study we utilize JEDI’s 50 to 1,000 keV electron- and 50 keV to >2,000 keV
 168 proton-measuring capabilities. The Jovian Auroral Distributions Experiment (JADE) measures
 169 thermal charged particle distributions. We utilize the JADE’s 3 to 30 keV electron (JADE-E) and
 170 0.5 to 46 keV/q ion (JADE-I) sensors for H^+ . JADE and JEDI complement one another to provide
 171 electron and proton energy and pitch angle spectra over a wide energy range. More details on the

172 instruments can be found in Mauk et al. (2017) and McComas et al. (2017), respectively. Science-
 173 ready data techniques and challenges are detailed in Mauk et al. (2020) and Allegrini (2020; 2021).

174 For the purpose of this study, we calculate the energy flux for electrons and H^+ (see Mauk et al.,
 175 2017; Clark et al., 2018; Allegrini et al., 2020). This is given by

$$Energy\ Flux = \pi \int_{E_{min}}^{E_{max}} I \cdot E dE \quad (1)$$

176 where I is the particle intensity ($cm^{-2} s^{-1} sr^{-1} keV^{-1}$), E is the electron energy (keV) and π is the
 177 area-projected-weighted size of the loss cone. The width of the loss cone is estimated as
 178 $arcsin(1/R^3)^{1/2}$, where R is the Jovicentric distance in Jovian radii.

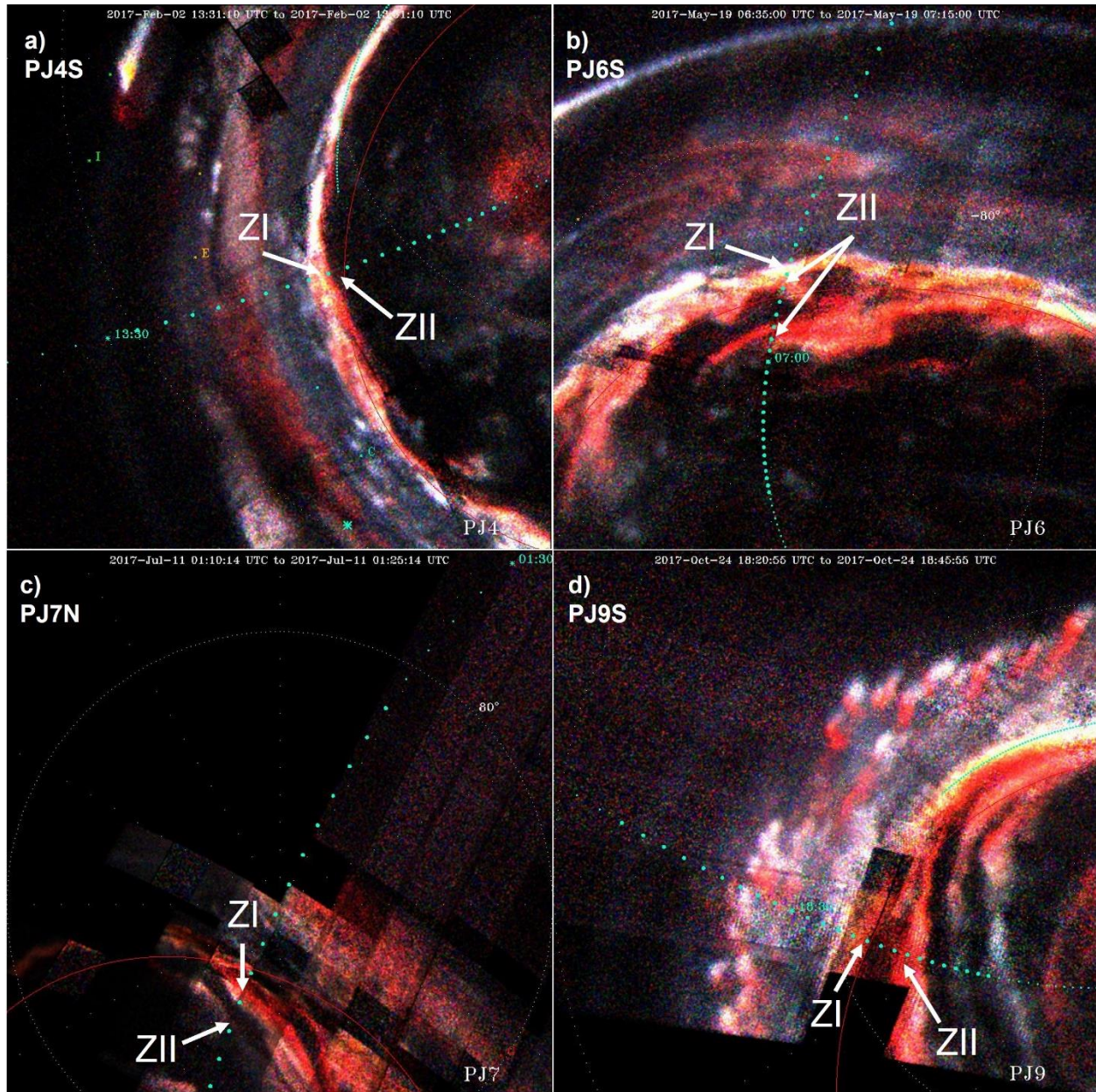
179 The magnetometer instrument (MAG) measures three components of the magnetic field and is
 180 used to determine the directionality of field-aligned currents inferred from azimuthal deflections
 181 in the magnetic field, δB_ϕ (Connerney et al., 2017). This is achieved by subtracting the modelled
 182 internal planetary field (Connerney et al., 2018) and slowly varying trends from the measurements,
 183 leaving out the deflections. The very high field strength compared to the average size of the
 184 deflections associated with the auroral currents poses challenges and this technique is thoroughly
 185 discussed by Kotsiaros et al. (2019). Furthermore, measured magnetic field fluctuations can be
 186 transformed into transverse and compressive components to identify the presence of Alfvén waves
 187 (Gershman et al., 2019). In our analysis, M-shells (magnetic shells for non-dipolar magnetic fields
 188 (McIlwain, 1961)) were calculated by field-line tracing using the JRM09 internal field model
 189 (Connerney et al., 2018) with a superimposed external current sheet model (Connerney et al.,
 190 1981).

191 The magnetic field measurements allow JADE and JEDI to order particle counts by pitch angle,
 192 thus allowing for particle directionality to be determined. Furthermore, the magnetic field strength
 193 is used by Waves to calculate the electron and proton cyclotron frequencies, f_{ce} and f_{cH^+} , and this
 194 allows for the species' temporal scales to be identified in spectrograms.

195 This study highlights datasets taken from the early part of *Juno*'s Prime Mission phase when the
 196 spacecraft's orbital plane was in the dawn sector (thereby sampling the dusk aurora near perijove).
 197 This is due to the approximate orthogonality between Jupiter's magnetic field and *Juno*'s spin
 198 vectors, which optimizes pitch angle coverage. The pitch angle coverage was compromised as
 199 *Juno*'s orbital plane migrated toward the nightside and will begin to improve as the migration
 200 continues into the dusk sector (and sample the dawn aurora near perijove) in the Extended Mission
 201 phase.

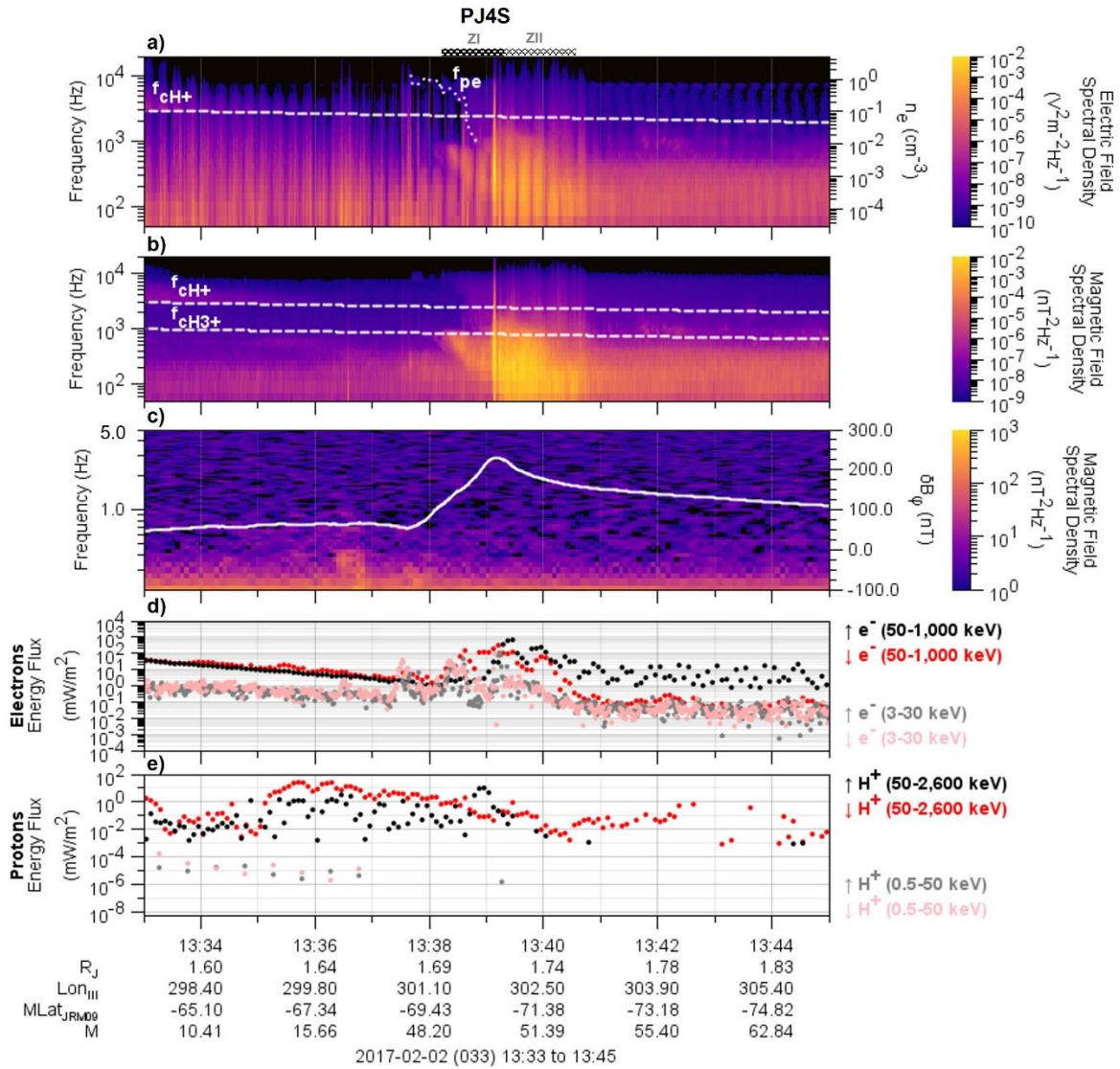
202 **3. Overview of Fields, Particles, and Plasma Waves in Jupiter's Auroral Zones**

203 We begin by providing an overview of the various fields, particles, and plasma wave phenomena
 204 observed when *Juno* was magnetically connected to (and equatorward of) Jupiter's auroral zones.
 205 We analyze four auroral passes which are shown in Figure 1 as ultraviolet (UV) images from the
 206 Ultraviolet Spectrograph instrument (Gladstone et al., 2017) with *Juno*'s magnetic footprint track
 207 overlaid. Figure 2 shows multi-instrument datasets recorded during *Juno*'s pass of Jupiter's
 208 southern aurora after its fourth perijove (PJ4S) corresponding to the aurora shown in Figure 1a.
 209 Figures 2a and 2b are electric and magnetic field frequency-time spectrograms, respectively, with



210 **Figure 1 – Orthographic projections of UV images of Jupiter’s aurora in false color for each**
 211 **event presented in Figures 2-5. Overlaid are magnetic footprint tracks of Juno separated by**
 212 **one minute.**

213 the H^+ and H_3^+ cyclotron frequency, f_{cH^+} and $f_{cH_3^+}$, overlaid. Throughout the time interval, f_{cH^+} and
 214 $f_{cH_3^+}$ were well within the frequency range of the Low Frequency Receiver (50-20,000 Hz). Such
 215 strong magnetic fields have not been previously met by spacecraft. Particularly for sampling
 216 auroral field lines, the strength of Jupiter’s magnetic field allows the Waves instrument to detect
 217 plasma waves at frequencies below f_{cH^+} and $f_{cH_3^+}$, and thus assess interactions with protons and
 218 heavy ions. Figure 2c is a spectrogram of the transverse (non-compressive) magnetic field power
 219 recorded by the magnetometer between 0.2 and 5 Hz (Gershman et al., 2019). Overlaid is the
 220 perturbation of Jupiter’s azimuthal magnetic field, δB_ϕ , after subtracting the JRM09 internal field
 221 model (Connerney et al., 2018). From Ampère’s law, significant gradients in the δB_ϕ perturbations



222

223 **Figure 2 – Plasma waves, fields, and charged particles when Juno was magnetically**
 224 **connected to Jupiter’s southern auroral zone near its 4th perijove (PJ4S). (a-b) Electric and**
 225 **magnetic field frequency-time spectrogram, respectively, measured by Waves. Overlaid onto**
 226 **each is the proton cyclotron frequency, f_{cH+} , as white dashed lines. The electron plasma**
 227 **frequency, f_{pe} , is digitized as the lower frequency cutoff of the Ordinary mode and shown as**
 228 **a white dotted line. The y-axis on the right converts f_{pe} in Hz to electron number density, n_e ,**
 229 **in cm^{-3} . (c) Transverse magnetic field fluctuations measured by MAG. Overlaid is the**
 230 **perturbation in the azimuthal magnetic field, δB_ϕ , as a white solid line. (d) Electron energy**
 231 **fluxes measured by JADE (light colors) and JEDI (dark colors) over the energy ranges 3-30**
 232 **keV and 50-1,000 keV, respectively. Black/gray and red/pink correspond to upward and**
 233 **downward populations, respectively. (e) Proton energy fluxes measured by JADE (light**
 234 **colors) and JEDI (dark colors) over the energy ranges 0.5-50 keV and 50-2,600 keV,**
 235 **respectively. Black/gray and red/pink correspond to upward and downward populations,**
 236 **respectively.**

237 are diagnostic of field-aligned currents (e.g., Kotsiaros et al., 2019). Figure 2d is a time series of
 238 the electron energy flux for the lower (3-30 keV) and higher (50-1,000 keV) energy ranges
 239 recorded by JADE and JEDI, respectively. These are specifically for populations within the loss
 240 cone and are differentiated between upward (away from Jupiter) and downward (toward Jupiter).
 241 Similarly, Figure 2e is a time series of the H^+ energy flux covering lower (0.5-50 keV) and higher
 242 (50-2,600 keV) energy ranges within the loss cone recorded by JADE and JEDI, respectively.

243 Describing the data from left to right along Juno's poleward trajectory, magnetic field lines
 244 threading Jupiter's diffuse aurora (DifA) were initially sampled, transitioning to Zone-I from
 245 13:38:15, then to Zone-II from 13:39:15 until 13:40:30, after which Juno was in the polar cap. The
 246 plasma wave spectra show significant wave power in both the E- and B-fields beginning as Juno
 247 entered Zone-I. Below f_{cH3+} , intense electromagnetic waves with a dispersive spectral character,
 248 i.e., a frequency dependence with time, extends throughout Zone-I. This is followed by an intense
 249 broadband electromagnetic emission that extends throughout Zone-II. There are jumps in both the
 250 low-frequency electric and magnetic field spectral densities at the boundary between Zone-I and
 251 Zone-II suggesting the mode is not continuous across. There are intermittent bursts of broadband
 252 emissions mostly in Zone-II. Above f_{cH+} and from equatorward of Zone-I, an electromagnetic
 253 emission is present with a clear lower frequency cutoff that is continuous across and throughout
 254 Zone-I. This lower frequency cutoff decreases non-monotonically until Zone-I and extends well
 255 below f_{cH+} . Of particular interest is the lack of a clear whistler-mode auroral hiss signature which
 256 exhibits a funnel shape above f_{cH+} and is a key plasma wave feature of planetary auroral regions
 257 (also commonly known as VLF saucers) (e.g., Gurnett et al., 1983).

258 The magnetic field data shows intense transverse fluctuations, interpreted as low-frequency Alfvén
 259 fluctuations, that extends throughout the region equatorward and stops short of Zone-I. There is
 260 likely some evidence of this fluctuation within Zone-I, albeit to a much lesser extent. However,
 261 this is near the low-frequency noise level and should be interpreted with care. The strongest field-
 262 aligned current, manifested as a large gradient in δB_ϕ perturbations in a narrow interval, marks the
 263 entry into Zone-I. Interestingly, this is clearly separated from the transverse fluctuations, which
 264 are largely equatorward of Zone-I. The δB_ϕ gradient is interpreted as an upward field-aligned
 265 current. In Zone-II the gradient reverses, but falls off much more slowly, indicating downward
 266 field-aligned current region that is extended over a larger region and is not as ordered and
 267 continuous as its Zone-I counterpart.

268 The electron energy flux shows bidirectional populations in both energy ranges equatorward of
 269 Zone-I and asymmetries emerge as Juno enters Zone-I. Just equatorward of the Zone-I boundary,
 270 there is a peak in the lower (3-30 keV) energy electron flux with more downward than upward
 271 fluxes. This is followed by a clear separation between the fluxes in the higher (50-1,000 keV)
 272 energy range in Zone-I with the downward energy fluxes dominating by up to $\sim 100\times$ compared to
 273 the upward energy fluxes. In Zone-II the asymmetry in the higher-energy electrons is clearly
 274 reversed, with greater upward energy fluxes than downward, also by $\sim 100\times$.

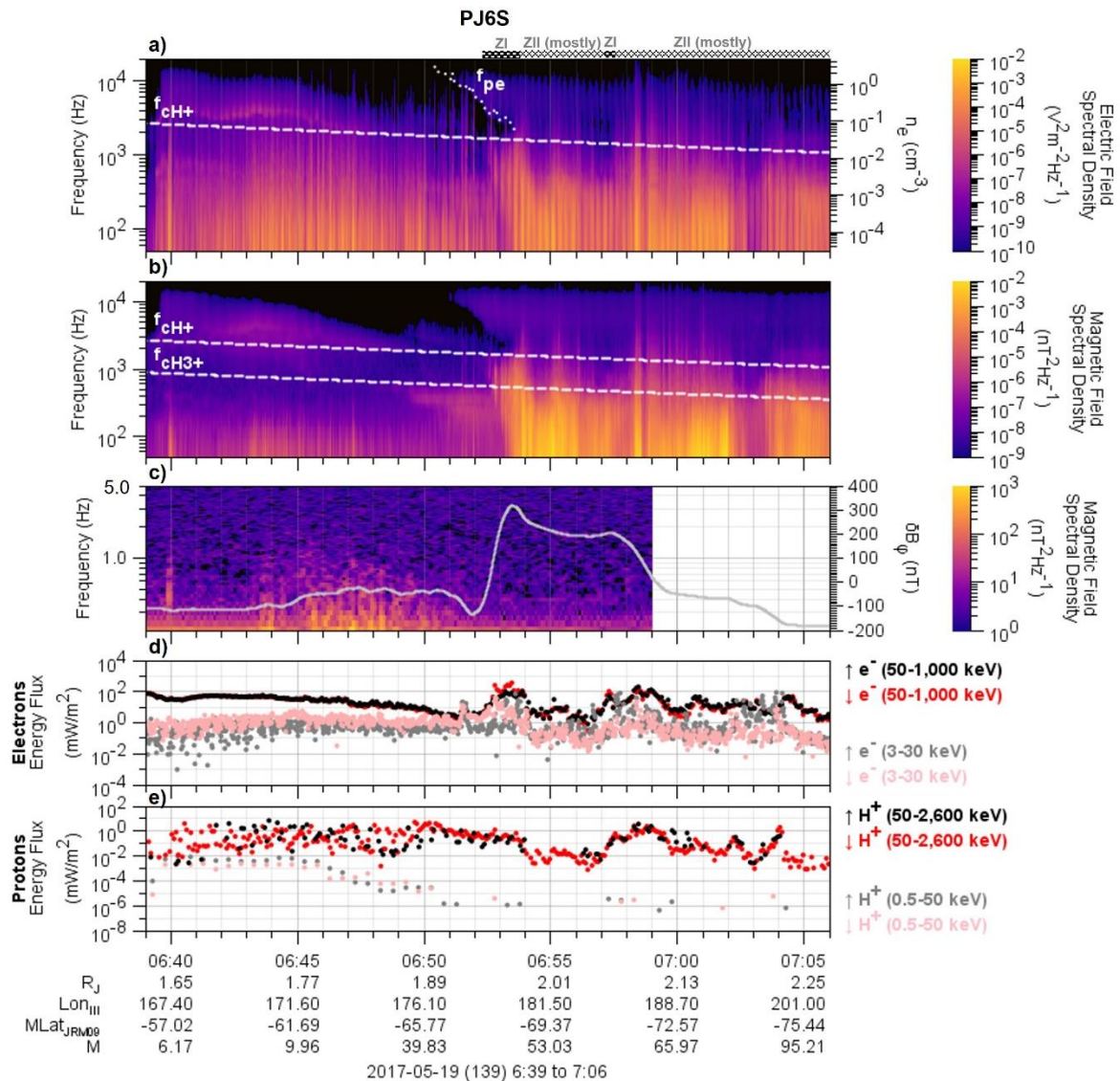
275 The data for H^+ energy fluxes are more limited in cadence compared to the electrons. In the higher
 276 (50-2,600 keV) energy population, there are episodes of bidirectionality, but the clearest feature is
 277 the dominant upward H^+ energy fluxes near 13:39 in Zone-I by $\sim 100\times$ compared to the downward
 278 energy fluxes.

279

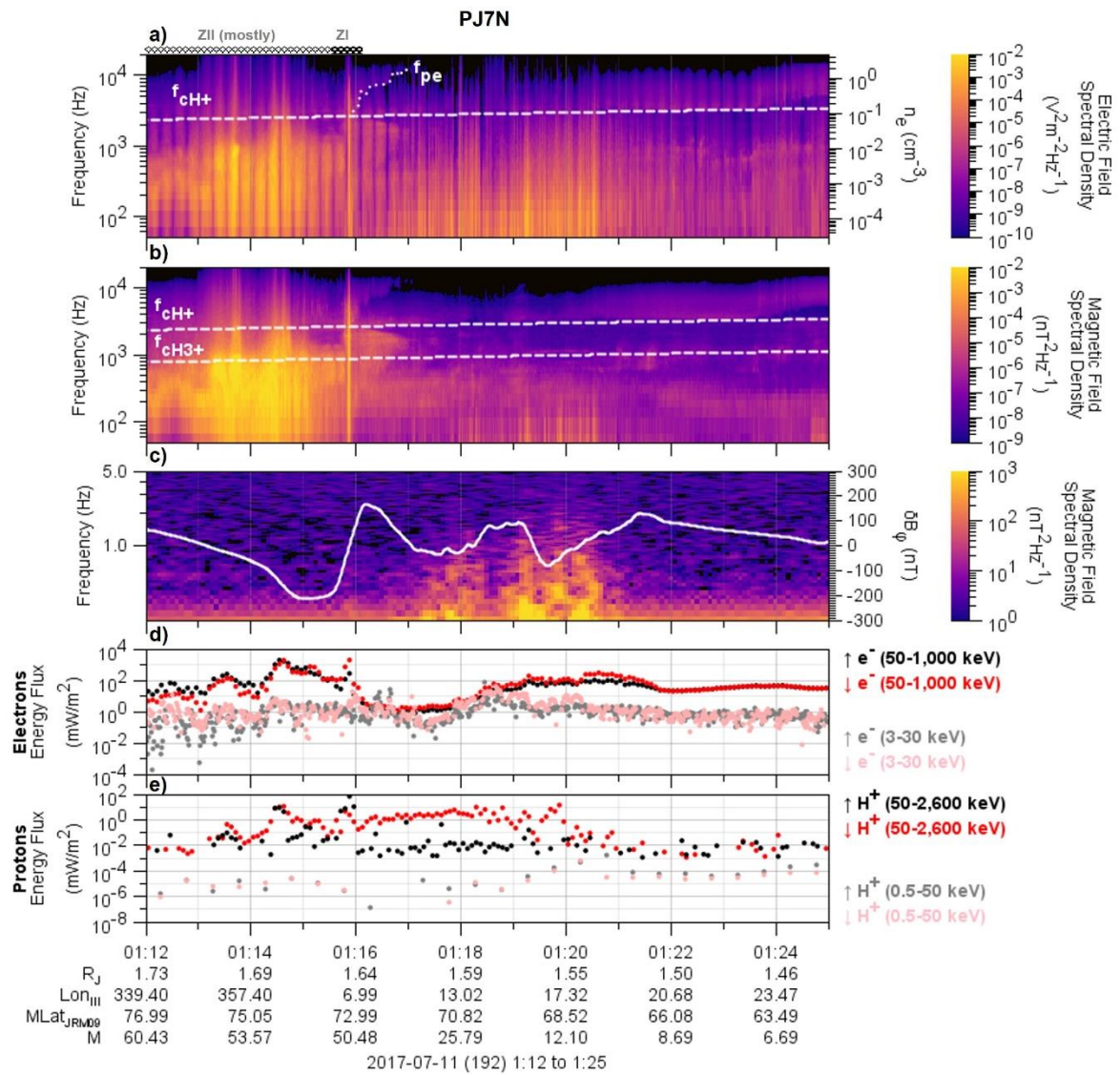
280 **4. Detailed Analysis and Discussion**

281 Various datasets have identified distinct features observed over Jupiter’s main aurora (e.g.,
 282 Gershman et al., 2019; Kotsiaros et al., 2019; Allegrini et al., 2020; Mauk et al., 2020; Szalay et
 283 al., 2017; 2021), however, these are yet to be analyzed altogether, and including a plasma wave
 284 analysis, to determine their association between the different zones and, more importantly, how
 285 they can be reconciled and fit into the bigger picture of Jupiter’s auroral generation mechanisms.

286 In addition to Figure 2 (PJ4S), we include three more multi-instrument time histories when Juno
 287 was magnetically connected to the auroral zones. These are shown in Figures 3-5 for PJ6S, PJ7N,
 288 PJ9S, respectively. The format is the same as that of PJ4S, noting that PJ7N is a northern pass and
 289 Juno was moving equatorward from left to right. Given the similarities that will be discussed, we
 290 do not go through each figure in detail but will highlight certain unique features where necessary.
 291 We focus our analysis on Zone-I and Zone-II, which are thought to carry the Birkeland currents.



292 **Figure 3 – Same as Figure 2 but for Jupiter’s southern auroral zone near its 6th perijove**
 293 **(PJ6S)**



294

295 **Figure 4 – Same as Figure 2 but for Jupiter’s northern auroral zone near its 7th perijove**
 296 **(PJ7N)**

297

298

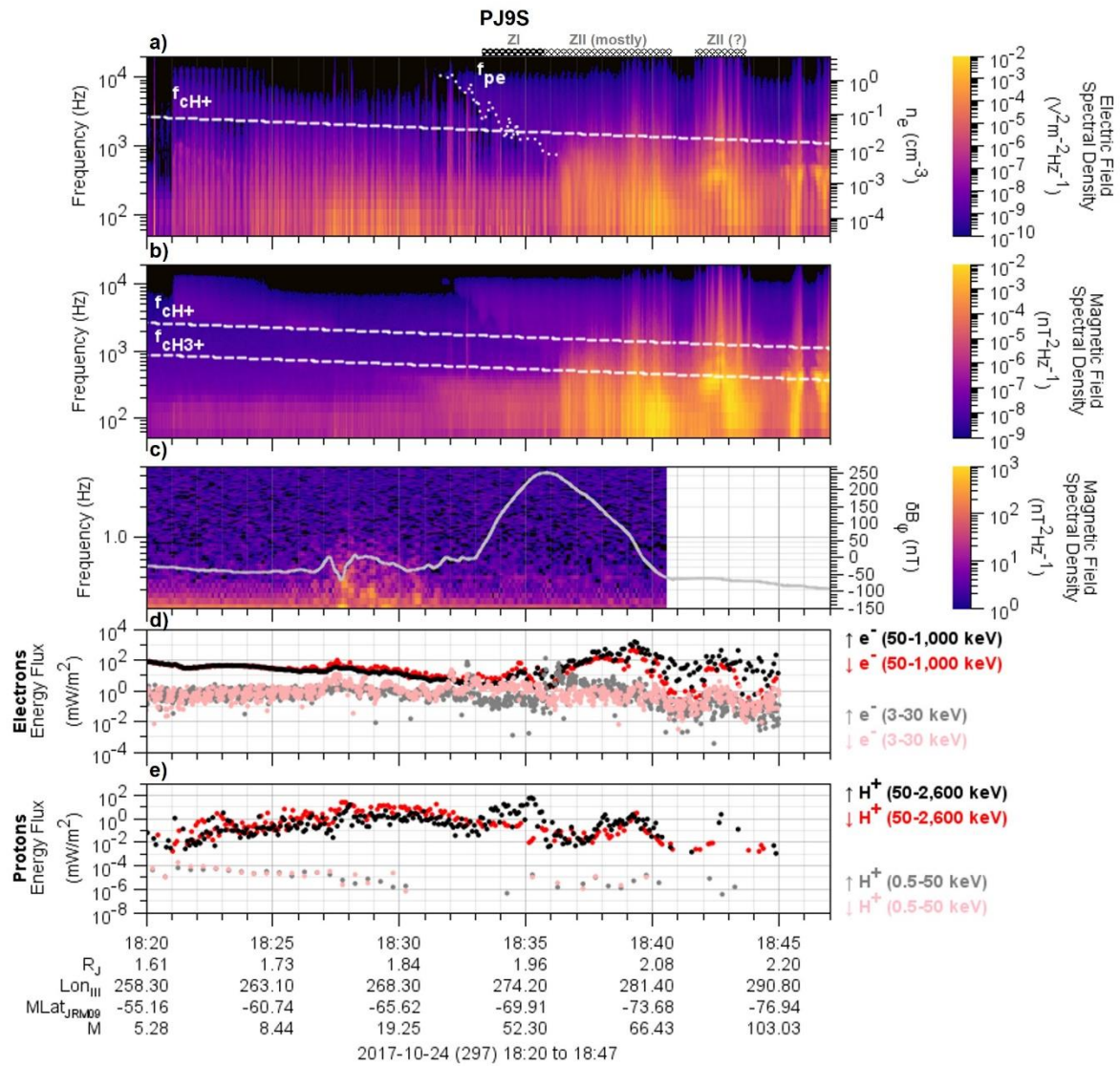
299

300

301

302

303



304

305 **Figure 5 – Same as Figure 2 but for Jupiter’s southern auroral zone near its 9th perijove**
 306 **(PJ9S)**

307 **4.1 Zone-I**

308 Zone-I occurs at intermediate latitudes just poleward of the diffuse aurora. The exact latitudes
 309 depend on hemisphere and local time. This region is by far the narrowest in latitude among the
 310 auroral zones as shown in Figure 1, but its clearly defined equatorward and poleward boundaries,
 311 as well as the high repeatability among the various datasets, make it the most straightforward to
 312 identify. Mauk et al. (2020) characterized this region with dominant downward energetic electrons
 313 within the loss cone.

314 Kotsiaros et al. (2019) and Mauk et al. (2020) noted an agreement between the upward field-
 315 aligned current and predominantly downward energetic electrons for the PJ6S auroral pass (shown
 316 here in Figure 3), suggesting that Zone-I is associated with upward electric currents. Figures 2-5

317 corroborate this correspondence between the 50-1,000 keV downward electrons and the well-
 318 structured upward field aligned current from δB_ϕ and confirm that most of the upward current is
 319 indeed carried by downward energetic electrons. It should be highlighted that although upward
 320 currents in Zone-I are well-ordered, the predominantly downward electron acceleration supporting
 321 these currents are via both inverted-V and broadband distributions, often the latter attaining higher
 322 energies (Mauk et al., 2017b). These distributions have been observed serially within the same
 323 Zone-I pass and are occasionally overlaid onto one another (see Figures 8 and 12 in Mauk et al.,
 324 (2020)). While the domination of the downward energetic electron is a reliable predictor of Zone-
 325 I, there exists large variability in the size of the asymmetry between the downward and upward
 326 energy fluxes among the different events. This can be as large as $100\times$ (e.g., PJ4S) and as relatively
 327 modest as $3\text{-}5\times$ (e.g., PJ6S and PJ9S). The size of the asymmetry is likely related to both the nature
 328 of the acceleration region and Juno's proximity to it.

329 Kurth et al. (2018) showed for PJ7N that an interval of downward broadband electron distribution
 330 (in what was later identified as Zone-I) is coincident with brief but very intense broadband plasma
 331 waves in both the electric and magnetic spectra ($\sim 01:15:51$ in Figure 4). It appears that this
 332 correspondence is repeatable across events whenever broadband distributions are present, e.g.
 333 $13:39:07$ during PJ4S in (Figure 2). There are, however, no plasma wave signatures that uniquely
 334 correspond to downward inverted V electron distributions. Kurth et al. (2018) proposed the
 335 importance of these intense broadband electromagnetic waves in intervals of broadband electron
 336 acceleration and determined the direction of their Poynting vector with respect to the Jovian
 337 magnetic field to show that they were propagating in the same direction as the predominant
 338 downward energetic electrons. These waves were interpreted as being in the whistler mode as the
 339 frequency extends well above f_{cH^+} and assumed to cut off at the electron plasma frequency, f_{pe} , at
 340 ~ 10 kHz (or $n_e \approx 1.2 \text{ cm}^{-3}$), which represents the theoretical upper frequency cutoff for whistler-
 341 mode waves in the presence of a strong magnetic field. We will show in the next section, however,
 342 that Zone-I is a region where the electron densities are dramatically depleted to as low as <0.01
 343 cm^{-3} , or $f_{pe} < 900$ Hz. Densities could not be inferred *within* these brief intervals of broadband
 344 acceleration, therefore the presence of the whistler mode would imply that the densities are
 345 anomalously greater during these intervals. Broadband electromagnetic waves are routinely
 346 observed over Earth's auroral regions, although typically confined to the downward current
 347 regions (Ergun et al., 1998b) and have also been reported in Jupiter's polar cap region (Elliot et
 348 al., 2020). We will revisit these features and show their correspondences against energy- and pitch-
 349 angle-time spectra when discussing Zone-II as they appear to be much more prevalent there.

350 Another important observation in Zone-I is the lack of, or significant reduction in, Alfvénic
 351 fluctuations compared to just equatorward in the diffuse aurora. Alfvén waves are known to
 352 develop parallel electric fields when finite electron mass is considered and their role has therefore
 353 been posited to explain the broadband nature of Jupiter's auroral electrons (Saur et al., 2018; Lysak
 354 et al., 2021). It is therefore likely that these waves have dissipated at higher Zone-I altitudes,
 355 lending most of their energy to electron acceleration. It is important to note that Jupiter's low-
 356 altitude region is characterized by very strong magnetic fields meaning any Alfvénic fluctuations
 357 present may just be too small to be picked up by the magnetometer. The Poynting flux is estimated
 358 as $\delta B^2 v_A / \mu_0$, where v_A is the Alfvén speed which considerably rises in the presence of sharp density
 359 depletions. Therefore, for a given Poynting flux, it follows that δB_ϕ would decrease
 360 correspondingly.

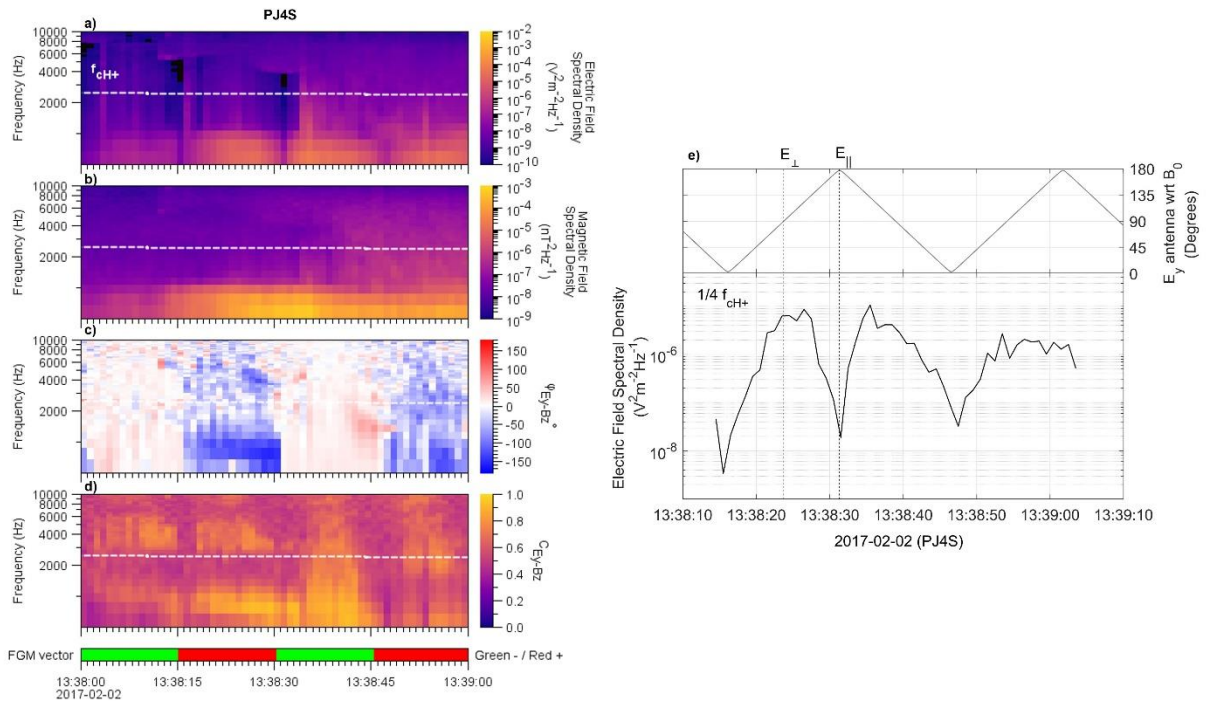
361 It is worth emphasizing that the Alfvénic fluctuations are repeatable signatures of the diffuse
 362 aurora, but not Zone-I or Zone-II. The waves are clearly supported over a wide range of M-shells.
 363 Allegrini et al. (2020) presented a survey showing that the lower-energy 3-30 keV electrons
 364 typically peak just equatorward of the main oval (or what is now called Zone-I). It appears from
 365 Figures 2-5 that the poleward edge of the Alfvénic fluctuations is when the 3-30 keV electrons
 366 peak and precedes the higher 50-1,000 keV that power Zone-I. Interestingly, during PJ4S and
 367 PJ7N (Figures 2 and 4) the Alfvénic fluctuations diminish as the 3-30 keV electron energy fluxes
 368 peak at ~13:37:30 and ~1:18:30, respectively, before recovering again. Li et al. (2021) applied a
 369 data-model comparison to show that whistler-mode waves are the driver of Jupiter’s diffuse auroral
 370 precipitation above several keV via pitch-angle scattering, although this mechanism did not
 371 account for the observed precipitation of lower energies (< several keV) and was limited to lower
 372 latitudes (M-shells 8-18). Based on our observed correspondences, we postulate that Alfvén waves
 373 may indeed be responsible for precipitating lower energy electrons in the diffuse aurora at the
 374 higher latitudes.

375 The most prominent plasma wave signature in Zone-I are intense emissions below f_{cH+} and f_{cH3+} .
 376 The electric and magnetic field spectral densities are enhanced over a broad range of low
 377 frequencies (few kHz bandwidth) and undergo a distinct drop in intensity at f_{cH+} and/or at f_{cH3+} .
 378 This is usually an indication of strong damping via cyclotron resonance where the wave energy is
 379 transferred to the corresponding ions. This characteristic is consistent with ion cyclotron waves
 380 and their observation in the presence of upward energetic ions and downward energetic electron
 381 beams draws a strong analogy to both Earth’s and Saturn’s upward current regions where the
 382 correlation has been observed (e.g., Cattell et al., 1988; McFadden et al., 1998; Mitchell et al.,
 383 2009; Bader et al., 2020). Ion cyclotron waves in the auroral regions have been observed as both
 384 electrostatic (EIC) and electromagnetic (EMIC) modes. The strong magnetic component here is
 385 evidence that EMIC waves are present, though not necessarily in the absence of EIC, and the
 386 significance is that they carry Poynting fluxes.

387 Figure 6a-d shows an analysis of the Poynting vector direction for these waves during PJ4S. These
 388 are the emissions present below 1 kHz and the series of peaks and nulls in the electric field
 389 spectrum is due to spin modulations. The electric and magnetic field fluctuations have high
 390 coherency, $C_{E_y-B_z} \approx 1$, and the combination of a phase $\phi_{E_y-B_z} \approx -180^\circ$ (or 180°) and a positive $B_x/|B_x|$
 391 in the southern hemisphere indicates an upward-propagating wave. Figure 6e shows that the power
 392 of these waves primarily resides perpendicular to the magnetic field. Here we compare the spin-
 393 modulations in the electric field spectral densities to the angle between the antenna dipole and
 394 background magnetic field and show that spectral densities peak (depress) when the antenna is
 395 perpendicular (parallel) to the magnetic field. At the measured frequency of $1/4 f_{cH+}$ the ratio of the
 396 components is $E_{\perp}/E_{\parallel} = 200$. Despite a strong magnetic component, the E/cB ratio (not shown here)
 397 is greater than one but of order unity. This can occur in the presence of an admixture of EIC and
 398 EMIC waves.

399 Although we cannot directly verify that they are intrinsically left-hand-polarized, we can indirectly
 400 infer this from the fact that their electric and magnetic fields are highly coherent, fluctuate
 401 perpendicular to the background magnetic field, and do not propagate above f_{cH+} or f_{cH3+} .
 402 Altogether, these are consistent with resonant absorption of left-hand-polarized ion cyclotron
 403 waves, a well-recognized mechanism for ion heating (e.g. André et al., 1998; Chang et al., 1986;
 404 Lysak, 1986). The observed (mostly) upward-propagation of these waves is somewhat in contrast
 405 to what is typically observed during low-altitude passes of Earth’s aurora, where waves below f_{cH+}

406 are more commonly observed to be downward propagating (Gurnett et al. 1984; Chaston et al.,
 407 1998). The difference at Jupiter may be either due to their sources originating at an altitude lower
 408 than Juno, i.e. $\lesssim 1 R_J$ above the one-bar level, or a different generation mechanism altogether.
 409 Electron drifts as the source of free energy driving ion cyclotron instability have been invoked to
 410 explain their correlation with auroral field-aligned currents (Cattell et al., 1998). Testing whether
 411 this hypothesis holds at Jupiter requires solving dispersion relations with modelled particle
 412 distributions which is beyond the scope of this study. It has been further demonstrated that
 413 broadband EMIC waves can also accelerate cold secondary electrons to form counterstreaming
 414 field-aligned electrons (McFadden et al., 1998). Since bidirectional electrons are a key feature of
 415 Jupiter's auroral zones, the role of EMIC waves should not be neglected.



416
 417 **Figure 6 – (left) Poynting vector analysis during PJ4S. (a-b) Electric and magnetic field**
 418 **frequency time spectrograms, respectively. (c-d) phase difference and coherence between**
 419 **measured electric and magnetic fields, respectively. (right) Angle between electric field**
 420 **antenna and background magnetic field correlated against the electric field spectral**
 421 **density at $1/4 f_{cH^+}$**

422 The coincident field-aligned H^+ fluxes suggest that any perpendicular heating by the ion cyclotron
 423 waves is not sufficient to deviate the pitch angle from the field-aligned direction and generate
 424 conics. The measured electric field spectral density of $10^{-5} V m^{-1} Hz^{-1}$ near f_{cH^+} (Figure 6e) yields
 425 a maximum cyclotron resonant heating rate of ~ 500 eV/s (Chang et al., 1986) and is comparable
 426 to that measured in Io's Main Alfvén Wing where, by contrast, H^+ conics were detected (Clark et
 427 al., 2020; Sulaiman et al., 2020). The difference is likely due to the interaction time, proximity to,
 428 nature of the acceleration region or a combination thereof. Szalay et al. (2021) concluded, based
 429 on the presence of H^+ inverted-V distributions, that quasi-static parallel potential structures drove
 430 the acceleration of H^+ away from Jupiter's high-latitude ionosphere. This is further supported by

431 the disappearance of upward H^+ during intervals of broadband acceleration within Zone-I shown
 432 by Mauk et al. (2018). The observation of both downward electron and upward H^+ beams at these
 433 altitudes would suggest that Juno was in or close to a unidirectional acceleration region, i.e., an
 434 upward parallel potential. Therefore, it is possible that the perpendicular heating supplied by ion
 435 cyclotron waves are overcome by the action of more powerful parallel potentials that deposit much
 436 larger amounts of energy along the field line. The ion cyclotron waves (shown to be upward
 437 propagating) may have their source in the ionosphere where the density is high and enough ions
 438 exist to significantly dampen the waves. Cold ionospheric ions are bound by Jupiter's large
 439 gravitational potential (the gravitation binding energy of H^+ is ~ 20 eV and H_3^+ is ~ 60 eV) and in
 440 order to be admitted into the electrostatic potential at higher altitudes, a means of energization is
 441 required to escape the gravitational potential. When ions are heated perpendicular to the magnetic
 442 field in the presence of a diverging magnetic field, they experience a mirror force that transports
 443 them to a region of weaker magnetic field, i.e., higher altitudes, as a parallel velocity component
 444 develops to conserve kinetic energy and the first adiabatic invariant.

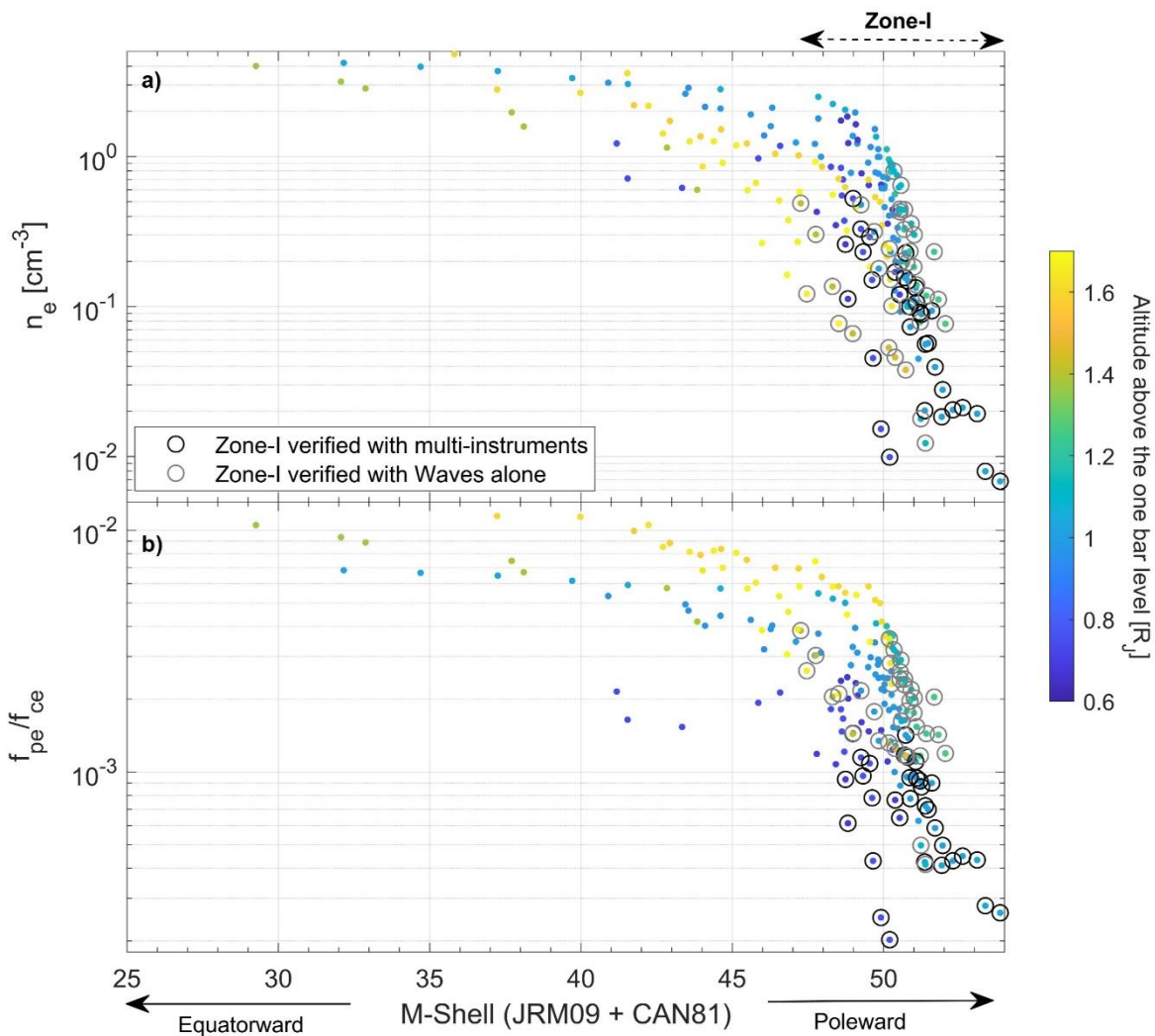
445 In summary, a multi-instrument in-situ analysis shows that the following criteria identify Zone-I
 446 in Jupiter's low-altitude auroral region: (i) presence of a gradient in the B_ϕ perturbation that is
 447 indicative of an upward field-aligned current, as measured by MAG; (ii) greater downward
 448 electron energy fluxes than upward, as well as greater than outside the loss cone, accompanied by
 449 inverted-V and/or broadband distributions as measured by JEDI; (iii) the low-frequency portion of
 450 intense, apparently dispersive, coherent, mostly upward-propagating ion (H^+ and/or H_3^+) cyclotron
 451 waves, as measured by Waves; and (iv) presence of field-aligned upward flowing H^+ accompanied
 452 by inverted-V distributions, as measured by JADE and JEDI. These observations are unique to
 453 Zone-I and highly repeatable, such that any one of them is highly predictive of Zone-I.
 454 Furthermore, they exhibit distinct and unambiguous equatorward and poleward edges that are
 455 consistent with the main oval emission shown in Figure 1. The boundary at which Alfvénic
 456 fluctuations significantly decrease reliably marks the entry into Zone-I from the diffuse aurora.
 457 The deficiency in observed Alfvénic fluctuations, however, is not a unique marker of Zone-I as
 458 this is continuous into Zone-II.

459 **4.2 Electron density depletions in Zone-I**

460 Electron density depletions occur within Zone-I, exhibiting large variability and with a sharply
 461 defined equatorward edge. The scatter plot in Figure 7a shows the electron number density
 462 variation with increasing M-shell. This is color-coded in altitude over a range of $0.6 - 1.7 R_J$ above
 463 the one-bar level. The direction of increasing M-shell translates into Juno sampling the auroral
 464 regions in the poleward sense, beginning with the equatorward edge of the broad diffuse aurora
 465 through to the poleward edge of Zone-I. The M-shells here are likely overestimated since the
 466 auroral regions are believed to be mapped to $\sim 30 R_J$ in the equatorial plane. The purpose of this
 467 figure is to examine how the electron densities vary on different field lines, including those mapped
 468 to the auroral zones. It should be noted that a different internal and/or current sheet models will
 469 yield different M-shell values. We therefore identify the auroral crossings based on *in-situ*
 470 observations and not rely on the values provided by M-shell mapping.

471 We digitize the densities by identifying Ordinary (O) mode waves that are sometimes present
 472 during the auroral passes (see Sulaiman et al. (2021) for the theoretical background as well as early
 473 and more recent implementations of this technique by Gurnett & Shaw (1973) and Elliott et al.
 474 (2021)). The waves are evanescent below f_{pe} and therefore exhibit a low frequency cutoff, as shown

475 in the first panels of Figures 2-5. Strictly speaking, this cutoff is an upper limit to the local electron
 476 plasma frequency due to the possibility of a higher-density region existing between the source and
 477 the spacecraft. When this occurs, the measured cutoff corresponds to the maximum density
 478 between the source and the spacecraft; however, the cutoffs observed here are usually well-defined
 479 and continuous which suggest the densities are local. Since $f_{pe} \propto \sqrt{n_e}$, the total electron number
 480 density is straightforwardly obtained and this is in excellent agreement with the electron partial
 481 density derived by JADE for overlapping intervals (see Figure S1). Despite the limited coverage
 482 in altitude shown here, the expected anti-correlation between density and altitude is present, giving
 483 confidence in our method. We obtain density measurements whenever the O-mode waves are
 484 present and discernible. The circled points highlight measurements taken when Juno was
 485 magnetically connected to Zone-I using all the criteria whenever the O-mode was present during
 486 the first 10 perijoves and only criteria (iii) thereafter, when the pitch angle coverage was
 487 suboptimal. Recall that any one of the criteria alone is a sufficient marker of Zone-I.



488

489 **Figure 7 – (a) Electron number density plotted against M-shell and color-coded with Juno’s**
 490 **altitude above Jupiter’s one-bar level. The circled data points are when Juno was**
 491 **magnetically connected to Zone-I. (b) f_{pe}/f_{ce} plotted against M-shell, same format as (a). The**

492 **M-shell was calculated using the JRM09 internal field model (Connerney et al., 2018) + an**
 493 **external current sheet model (Connerney et al., 1981). This is likely overestimating the true**
 494 **M-shell.**

495 Figure 7a exposes a sharply defined boundary between the diffuse aurora and Zone-I. Within Zone-
 496 I, the electron densities deplete steeply by up to two orders of magnitude down to below 0.01 cm^{-3}
 497 ³. In Zone-II, the sub- f_{CH+} band of the O-mode waves become “washed out” in the spectrogram
 498 due to the presence of intense broadband low-frequency electromagnetic emissions, therefore it is
 499 not possible to determine, based on this technique, how far they remain depleted and
 500 whether/where they steeply recover. All Zone-I verified densities are below 0.1 cm^{-3} with a subset
 501 below 0.01 cm^{-3} .

502 Density depletions are known to be intimately related to auroral acceleration processes (e.g.,
 503 Persoon et al., 1998; Paschmann et al., 2003) and are in fact a prerequisite. Their association is
 504 well supported by theoretical modelling (Block and Fälthammar, 1968; Knight, 1973) and
 505 repeatedly corroborated by experimental evidence (Ergun et al., 2002; Hull et al., 2003) although
 506 much of the focus has been on the development of parallel potentials in the context of inverted V
 507 distributions. The basic principle is that density depletions reduce the number of charge carriers
 508 thereby limiting the ability of plasmas to carry strong field-aligned currents. This “current choke”
 509 results in the development of parallel electric fields as the displacement current term of Ampère’s
 510 law builds up to ensure $\nabla \times \mathbf{B}$ is balanced (Song and Lysak, 2006; Ray 2009).

511 Although turbulence-induced broadband processes are typically associated with weaker Alfvénic
 512 aurora at Earth, they are believed to be of at least equal importance in generating Jupiter’s most
 513 intense aurora (Clark et al., 2018; Saur et al., 2018). Parallel electric fields from Alfvén waves
 514 become important when the $k_{\perp}^2 \lambda_e^2$ term is large, where λ_e is the electron inertial length given by
 515 $c/2\pi f_{pe}$ and k_{\perp} is the wave vector component perpendicular to the background magnetic field. A
 516 large k_{\perp} can be satisfied by a converging flux tube as the area is inversely proportional to B . A
 517 low-density region, or greater λ_e , means Alfvén waves undergoing a turbulent cascade are
 518 dissipated ‘earlier’ in k -space. The measured densities in Zone-I equate to λ_e as large as 50 km,
 519 larger than 20-30 km modelled by Saur et al. (2018), thereby further lowering the threshold for
 520 Alfvénic dissipation to be achieved in the high-latitude region. Dispersive Alfvén waves have been
 521 observed within deep density cavities over Earth’s auroral oval together with upgoing transversely
 522 heated ionospheric ions and downgoing field-aligned electrons. This has been interpreted as
 523 evidence for a positive feedback mechanism, whereby small-scale Alfvén waves erode the auroral
 524 ionosphere by facilitating ion outflow, which in turn leads to deeper density cavities that maintain
 525 the production of small-scale Alfvén waves via refraction and phase mixing of incoming large-
 526 scale Alfvén waves (Rankin et al., 1999; Chaston et al., 2006). More recently, Lysak et al. (2021)
 527 proposed that an ionospheric Alfvénic resonator (IAR) operating at Jupiter can account for the
 528 observed broadband electron distributions. This is a widely accepted model used to explain similar
 529 distributions in the case of Earth, whereby the propagation of Alfvén waves is facilitated by a rapid
 530 decrease in density (Lysak et al., 1991). The corresponding increase in Alfvén speed gives rise to
 531 partial reflection of Alfvén waves which become trapped. At large enough k_{\perp} , the parallel electric
 532 field fluctuating at some resonant frequency can result in electron acceleration over a broad range
 533 of energies.

534 Figure 7b combines the electron densities with measured magnetic field strengths to express f_{pe}/f_{ce}
 535 variations. This ratio is especially important for the generation of radio emissions via the Cyclotron

536 Maser Instability (Wu & Lee, 1979). This mechanism requires $f_{pe}/f_{ce} \ll 1$ in the presence of a
 537 positive gradient in the perpendicular velocity distribution of weakly relativistic electrons. It is
 538 clear that the necessary low f_{pe}/f_{ce} is well satisfied, particularly in Zone-I, thus will provide further
 539 constraints on Jupiter's radio sources (e.g. Imai et al., 2019; Louis et al., 2019).

540 **4.3 Zone-II**

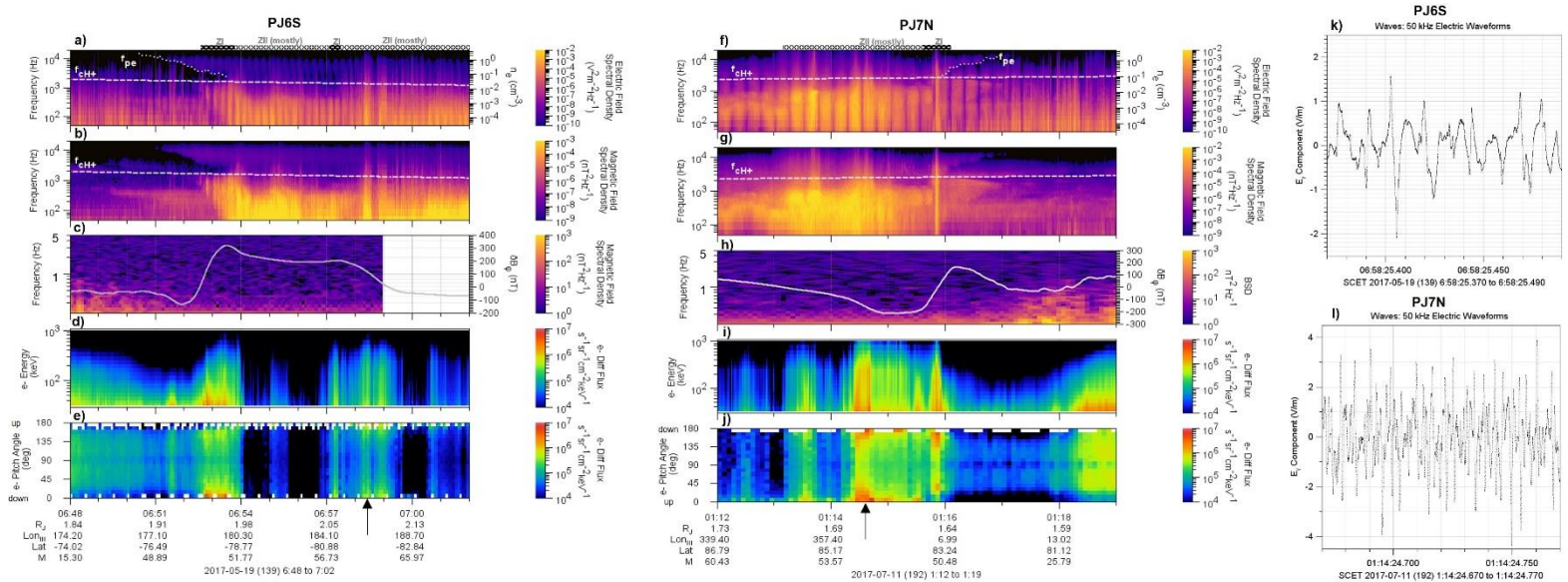
541 Among the three zones, Zone-II occurs at the highest latitudes just poleward of Zone-I. This region
 542 has a clearly defined equatorward boundary, but its poleward boundary with the polar cap is often
 543 ambiguous. Mauk et al. (2020) characterized this region with upward energetic electrons with
 544 energy fluxes greater than or equal to the downward component within the loss cone. Another key
 545 difference is the bidirectional electrons are almost always broadband in energy. On the other hand,
 546 downward H^+ inverted-Vs have been observed intermittently and, by contrast to Zone-I's highly
 547 field-aligned H^+ beams, exhibit a nearly isotropic pitch angle distribution with an empty upward
 548 loss cone (Mauk et al., 2020). Whereas Zone-I features are typically (but not always) continuous
 549 within its boundaries, Zone-II features are spatially or temporally sporadic.

550 Kotsiaros et al. (2019) and Mauk et al. (2020) noted agreements between the downward field-
 551 aligned currents and Zone-II during the PJ6S auroral pass (Figure 3), although this is usually
 552 limited to the most intense portion of the energetic particles and not as simple as the ordering for
 553 Zone-I. Again, Figures 2-5 corroborate this correspondence. Observed Alfvénic fluctuations in
 554 Zone-II remain relatively low/absent and comparable to Zone-I. This could also be evidence of
 555 dissipation, especially in a region supported predominantly by broadband, bidirectional energetic
 556 electrons (Saur et al., 2018; Lysak et al., 2021) and in the absence of strong evidence for inverted-
 557 Vs and thus local parallel potentials. The plasma wave emissions, on the other hand, are the most
 558 intense of all zones with the largest average amplitudes in both the electric and magnetic fields.
 559 These are present throughout Zone-II and majority of the power is confined to frequencies below
 560 f_{cH^+} (Figures 2-5), and are often accompanied by brief, intense emissions that extend well above
 561 f_{cH^+} that resemble those sometimes observed in Zone-I. The difference is that these brief and
 562 intense emissions occur intermittently in Zone-I whereas they appear to be a key feature of Zone-
 563 II and are correlated with the intervals of most intense energetic electrons which are in turn
 564 correlated with downward currents.

565 The downward current region is fundamentally different from its upward counterpart. The charge
 566 carriers are abundantly sourced from the cold, dense ionosphere as electrons and are accelerated
 567 by many orders of magnitude above their thermal energy. What is peculiar about Jupiter's Zone-
 568 II is that although the downward electron energy fluxes are generally no greater than the upward
 569 energy fluxes, they can be as intense or greater than the downward energy fluxes in Zone-I and
 570 sufficient to produce observable auroras (Mauk et al., 2020; and see Figure 1 here), in contrast to
 571 the "black aurora" at Earth and Saturn that are connected to flux tubes carrying downward currents.
 572 It is clear based on the difference in fields and particles characteristics that the acceleration
 573 mechanism in Zone-II is distinct and more observationally complicated than that supporting Zone-
 574 I. While Juno does not carry a DC electric field instrument, the various characteristics highlighted
 575 in the previous section support the sporadic presence (although not exclusively) of parallel
 576 potential structures in Zone-I. Other than the downward H^+ inverted Vs that are sometimes
 577 observed in Zone-II and not least that they are quasi-isotropic, the evidence for a stable parallel
 578 potential is inconclusive. The bidirectional electrons might be interpreted as originating from

579 potential structures above and below the spacecraft, however, this is not consistent with their
 580 broadband energy.

581 We emphasized in the previous section that EMIC waves should not be neglected in the context
 582 of electrons since their link has been established (McFadden et al., 1998), whereby cold secondary
 583 electrons are trapped and accelerated to form counterstreaming populations. It is therefore
 584 probably not a coincidence that the most intense waves below f_{CH+} occur in Zone-II, where
 585 bidirectional electrons are present.



586 **Figure 8 – Plasma waves, fields, and charged particles when Juno was magnetically**
 587 **connected to Jupiter’s southern auroral zone near its 4th perijove (PJ4S, left) and Jupiter’s**
 588 **northern auroral zone near its 7th perijove (PJ7N, right). (a/f) Electric and (b/g) magnetic**
 589 **field frequency-time spectrogram measured by Waves. Overlaid onto each is the proton**
 590 **cyclotron frequency, f_{CH+} , as white dashed lines. The electron plasma frequency, f_{pe} , is**
 591 **digitized as the lower frequency cutoff of the Ordinary mode and shown as a white dotted**
 592 **line. The y-axis on the right converts f_{pe} in Hz to electron number density, n_e , in cm^{-3} . (c/h)**
 593 **Transverse magnetic field fluctuations measured by MAG. Overlaid is the perturbation in**
 594 **the azimuthal magnetic field, δB_ϕ , as a white solid line. (d/i) 50-1,000 keV electron energy-**
 595 **time and (e/j) pitch-angle-time spectrograms measured by JEDI. The depletion near 90° is**
 596 **likely due to spacecraft shadowing and therefore not real. (k/l) Electric field waveforms**
 597 **corresponding to the times indicated by black arrows in stack plots.**

598 An important piece of the puzzle for broadband electrons may be in the contemporaneous
 599 broadband emissions shown in Figure 8. In the frequency domain, large-amplitude solitary
 600 structures (or “spiky” features) in the waveform manifest as broadband noise. Electrostatic solitary
 601 waves (ESWs) have been proposed to play a key role in accelerating electrons by carrying
 602 substantial potentials and are most often observed in Earth’s downward current regions and in the
 603 presence of density depletions (Ergun et al., 1998b; Temerin et al., 1982). The ubiquity of these
 604 broadband emissions in Zone-II might be explained by the highly nonlinear evolution of two-
 605 stream electron beam instabilities, set up by bidirectional populations, that give rise to sharp pulses

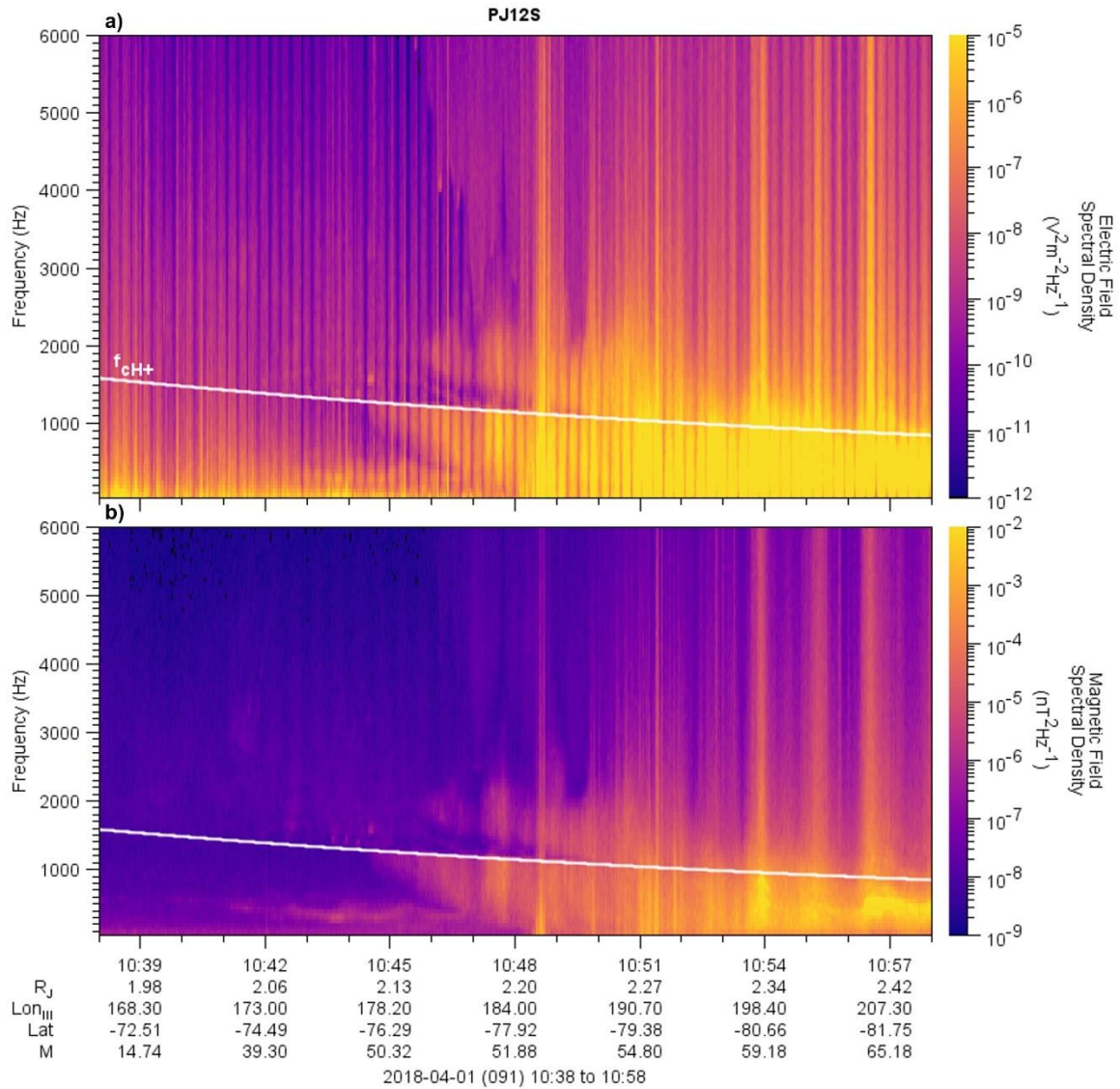
606 in the electric field (Matsumoto et al., 1994), as shown in Figure 8. Field-aligned electrons are then
 607 accelerated to a broad range of energies by the sum of individual micro-potential drops as they
 608 travel through ESWs. Despite their electrostatic nature, it is possible to measure an associated
 609 magnetic component (not shown here) which would result from the Lorentz field of a travelling
 610 charge.

611 Although the electron densities cannot be inferred within Zone-II, we can say with reasonable
 612 confidence that they remain low. The O-mode emissions above f_{cH^+} appear continuous well into
 613 Zone-II with its low frequency edge in the region below f_{cH^+} that is dominated by intense
 614 electromagnetic turbulence. We therefore set f_{cH^+} to be the approximate upper limit of f_{pe} and
 615 conclude that the electron densities within Zone-II are $< 0.1\text{-}0.01\text{ cm}^{-3}$. Therefore, the
 616 correspondingly large electron inertial lengths in Zone-II would similarly lower the threshold for
 617 Alfvénic dissipation, which remains the leading mechanism to account for the observed electron
 618 spectra (Saur et al., 2018; Lysak et al., 2021). Whether the densities are comparable to Zone-I, of
 619 similar variability and/or spatial scales are important questions that are beyond the reach of our
 620 current digitization methods.

621 Perhaps the most recognizable and commonly observed plasma wave feature above auroral regions
 622 is the whistler-mode auroral hiss. In a frequency-time spectrogram, they are easily identified by
 623 their characteristic funnel or V-shape (Gurnett, 1966; James 1976) which arises when the wave
 624 normal angle approaches the whistler-mode resonance cone (Santolík and Gurnett, 2002). The
 625 favored generation mechanism is a coherent beam-plasma instability at the Landau velocity
 626 (Maggs, 1976; Farrell et al., 1989), i.e., $\omega/k_{\parallel} \approx v_{\parallel}$. Since the auroral regions, including satellite
 627 auroral flux tubes, are a site for electron beams, whistler-mode auroral hiss are often observed and
 628 are often a reliable diagnostic for field-aligned currents (Gurnett et al. 1983; 2009; Sulaiman et al.,
 629 2018; 2020). That said, these plasma wave features are not as clearly identifiable in Jupiter’s low-
 630 altitude auroral zones, contrary to expectation.

631 Figure 9 shows a rare example when this was observed in the southern auroral zone during PJ12S.
 632 Although it appears like there are two similar emissions above and below f_{cH^+} , they are
 633 fundamentally different and not connected since, above f_{cH^+} , the timescales fall below the ion
 634 gyroperiod and the ions are effectively unmagnetized. Typically, whistler-mode auroral hiss is not
 635 seen to propagate down to as low as f_{cH^+} . Along the resonance cone, the lower hybrid frequency,
 636 f_{LH} , represents a lower limit through which they cannot propagate but instead reflect. In this highly
 637 magnetized regime, i.e., $f_{ce} \gg f_{pe}$, we find $f_{LH} \simeq f_{cH^+}$ (Sulaiman et al., 2021) and therefore conclude
 638 the waves are reflecting at the f_{cH^+} boundary. While the whistler mode is typically observed as
 639 electromagnetic, its propagation along the resonance cone is quasi-electrostatic and this is
 640 supported by the relatively weaker magnetic component and an E/cB ratio of ~ 10 . This mode is
 641 characterized by an index of refraction that is much greater than unity, i.e., a phase velocity that is
 642 low. Therefore, the Landau resonance condition requires low-energy electrons for the beam-
 643 plasma instability. Higher-energy electrons that interact with higher phase velocities can generate
 644 electromagnetic waves that cease to exhibit the characteristic funnel-shape. And even higher
 645 energies that exceed the maximum phase speed allowed by the dispersion relation will result in no
 646 Landau resonance altogether. This likely explains why quasi-electrostatic auroral hiss is not as
 647 common a feature at Jupiter’s low-altitude region as at Earth or Saturn owing to the much higher
 648 electron energies at play.

649



650

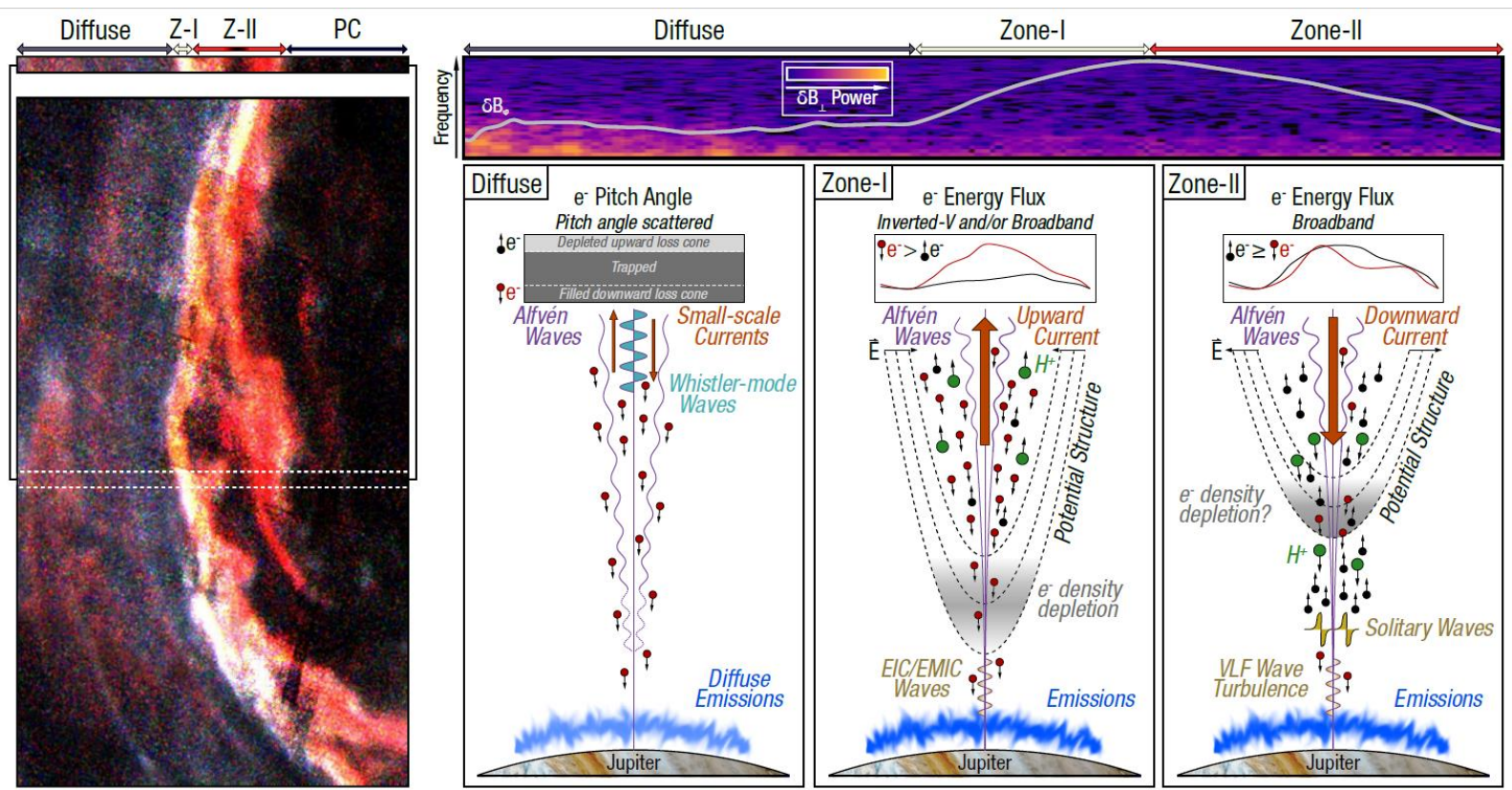
651 **Figure 9 – (a) Electric and (b) magnetic field frequency-time spectrograms when Juno was**
 652 **magnetically connected to Jupiter’s southern auroral zone near its 12th perijove (PJ12S)**
 653 **showing the characteristic funnel-shaped whistler-mode auroral hiss above f_{cH+} .**

654 Finally, what has not been covered in this study are the properties of heavy ions. The clear cutoff
 655 of plasma waves in *Zone-I* at f_{cH3+} is indicative of H_3^+ cyclotron waves and is strong (indirect)
 656 evidence for presence of upward H_3^+ . However, H_3^+ ions in the auroral zones have not been
 657 reported by the particle instruments at the time of writing. The presence of multiple heavy ions
 658 would have a significant impact since each additional ion introduces five characteristic
 659 frequencies: the standard cyclotron and plasma frequencies plus the more complex ion hybrid,
 660 multi-ion cutoff, and crossover frequencies, which require numerical solving. The latter three are
 661 highly sensitive to the fractional abundance of ions, let alone any individual density. This also
 662 means that composition can be constrained by modelling and correctly diagnosing wave modes
 663 and their characteristic frequencies. The significance of an ion hybrid frequency in a

664 multicomponent plasma is that it modifies the wave mode’s dispersion relation and therefore how
 665 it propagates through the medium. For example, a resonance cone can develop above each hybrid
 666 frequency (Santolík et al., 2016). The crossover frequency is that which the waves reverse their
 667 intrinsic polarization (left to right or vice versa) and can therefore affect the nature of wave-particle
 668 interactions.

669 5. Summary and Conclusions

670 We have provided a multi-instrument analysis on Jupiter’s low-altitude Zone-I and Zone-II. Figure
 671 10 is a graphical listing of the various observables identified in Zone-I and Zone-II, with the caveat
 672 that these structures are likely more complex and may exhibit considerable spatial and/or temporal
 673 variability, for example during transient episodes like dawn storms (Bonfond et al., 2021; Ebert et
 674 al., 2021). As the spacecraft migrates to afford coverage of the low-altitude dawn aurora, spatial
 675 variability of the fields, particles, and plasma wave features will likely arise.



676 **Figure 10 – Graphic illustrating the average picture of the fields, particles, and plasma waves**
 677 **in Jupiter’s low-altitude diffuse aurora, Zone-I, and Zone-II.**

678 Our main conclusions are:

- 679 • Zone-I and Zone-II are corroborated to be associated with the upward and downward
 680 current regions, respectively.
- 681 • Alfvénic fluctuations are most profoundly observed in the diffuse aurora and not in Zone-
 682 I and Zone-II. In the diffuse aurora, they intermittently diminish where 3-30 keV electron
 683 energy fluxes peak and are mostly absent in the Zone-I and Zone-II, where 50-1,000 keV

684 electron energy fluxes dominate. We suggest that this pattern is consistent with Alfvénic
 685 dissipation at higher altitudes.

- 686 • The features of Zone-I are typically coherent across all fields, particles, and plasma wave
 687 observations. The equatorward and poleward boundaries are well defined.
- 688 • The features of Zone-II are typically episodic across all observables. The equatorward edge
 689 (with Zone-I) is well defined but the poleward edge with the polar cap can often be
 690 ambiguous.
- 691 • The most prominent plasma wave modes are below the H^+ and H_3^+ cyclotron frequencies,
 692 f_{cH^+} and $f_{cH_3^+}$. Electromagnetic ion cyclotron waves, and possibly including electrostatic
 693 waves, are commonly observed in Zone-I and in the presence of H^+ beams. They are
 694 typically upward propagating and fluctuate perpendicular to the magnetic field. We
 695 interpret them as the means by which gravitationally bound H^+ and H_3^+ can be energized
 696 and admitted into a parallel potential at higher altitudes.
- 697 • Low-frequency plasma waves in Zone-II are the most intense. Electromagnetic emissions
 698 are also prevalent in Zone-II where broadband energetic electrons peak, which is in turn
 699 correlate with deflections in δB_ϕ . These are prevalent in Earth's downward current regions.
 700 We demonstrate that they are a result of large-amplitude solitary waves. These have
 701 previously been shown to be the stable end-result of a two-stream instability and are
 702 capable of supporting parallel potentials (Matsumoto et al., 1994). We therefore suggest
 703 this likely explains their presence in a zone dominated by bidirectional populations.
- 704 • Using plasma wave spectra, large-scale electron density depletions are identified over the
 705 auroral zones with a sharp boundary between the diffuse aurora and Zone-I. These
 706 depletions are critical for the development of high-latitude parallel potentials, Alfvénic
 707 dissipation, and radio wave generation.

708

709 **Acknowledgements**

710 The authors gratefully acknowledge J. Faden and the use of Autoplot. The research at the
 711 University of Iowa was supported by NASA through contract 699041X with the Southwest
 712 Research Institute. OS acknowledges support from the LTAUSA17070 project and from the
 713 Praemium Academiae Award. The Waves, JADE, MAG, and JEDI data used in this article have
 714 the Dataset ID JNO-E/J/SS-WAV-3-CDR-BSTFULL-V1.0, JNO-J/SW-JAD-3-CALIBRATED-
 715 V1.0, JNO-J-3-FGM-CAL-V1.0, and JNO-J-JED-3-CDR-V1.0 respectively and are publicly
 716 accessible through the Planetary Plasma Interactions Node in the Planetary Data System
 717 (<https://pds-ppi.igpp.ucla.edu/>). In this paper we use an effective E-field antenna length of 0.5 m.

718

719

720

721

722

723 **References**

- 724 Allegrini, F., Bagenal, F., Bolton, S., Connerney, J., Clark, G., Ebert, R. W., et al. (2017).
 725 Electron beams and loss cones in the auroral regions of Jupiter. *Geophysical Research*
 726 *Letters*, 44(14), 7131–7139. <https://doi.org/10.1002/2017GL073180>
- 727 Allegrini, F., Gladstone, G. R., Hue, V., Clark, G., Szalay, J. R., Kurth, W. S., et al. (2020a).
 728 First Report of Electron Measurements During a Europa Footprint Tail Crossing by
 729 Juno. *Geophysical Research Letters*, 47(18), e2020GL089732.
 730 <https://doi.org/https://doi.org/10.1029/2020GL089732>
- 731 Allegrini, F., Kurth, W. S., Elliott, S. S., Saur, J., Livadiotis, G., Nicolaou, G., et al. (2021).
 732 Electron Partial Density and Temperature Over Jupiter’s Main Auroral Emission Using Juno
 733 Observations. *Journal of Geophysical Research: Space Physics*, 126(9), e2021JA029426.
 734 <https://doi.org/10.1029/2021JA029426>
- 735 André, M., et al. (1998), Ion energization mechanisms at 1700 km in the auroral region, *Journal*
 736 *of Geophysical Research*, 103, A3, doi:10.1029/97JA00855
- 737 Auroral density fluctuations on dispersive field line resonances. (1999). *Journal of Geophysical*
 738 *Research: Space Physics*, 104(A3), 4399–4410. <https://doi.org/10.1029/1998JA900106>
- 739 Bader, A., Badman, S. V., Ray, L. C., Paranicas, C. P., Lorch, C. T. S., Clark, G., et al. (2020).
 740 Energetic Particle Signatures Above Saturn’s Aurorae. *Journal of Geophysical Research: Space*
 741 *Physics*, 125(1), e2019JA027403. <https://doi.org/10.1029/2019JA027403>
- 742 Block, L. P., & Fälthammar, C.-G. (1968). Effects of field-aligned currents on the structure of
 743 the ionosphere. *Journal of Geophysical Research* (1896-1977), 73(15), 4807–4812.
 744 <https://doi.org/10.1029/JA073i015p04807>
- 745 Bonfond, B., Gladstone, G. R., Grodent, D., Greathouse, T. K., Versteeg, M. H., Hue, V., et al.
 746 (2017). Morphology of the UV aurorae Jupiter during Juno’s first perijove
 747 observations. *Geophysical Research Letters*, 44(10), 4463–4471.
 748 <https://doi.org/10.1002/2017GL073114>
- 749 Bonfond, B., Yao, Z. H., Gladstone, G. R., Grodent, D., Gérard, J.-C., Matar, J., et al. (2021).
 750 Are Dawn Storms Jupiter’s Auroral Substorms? *AGU Advances*, 2(1), e2020AV000275.
 751 <https://doi.org/10.1029/2020AV000275>
- 752 Carlson, C. W., Pfaff, R. F., & Watzin, J. G. (1998). The Fast Auroral SnapshoT (FAST)
 753 Mission. *Geophysical Research Letters*, 25(12), 2013–2016. <https://doi.org/10.1029/98GL01592>
- 754 Cattell, C., Bergmann, R., Sigsbee, K., Carlson, C., Chaston, C., Ergun, R., et al. (1998). The
 755 association of electrostatic ion cyclotron waves, ion and electron beams and field-aligned
 756 currents: FAST observations of an auroral zone crossing near midnight. *Geophysical Research*
 757 *Letters*, 25(12), 2053–2056. <https://doi.org/10.1029/98GL00834>
- 758 Chang, T., et al. (1986), Transverse acceleration of oxygen ions by electromagnetic ion cyclotron
 759 resonance with broad band left-hand polarized waves, *Geophysical Research Letters*, 13,
 760 doi:10.1029/GL013i007p00636

- 761 Chaston, C. C., Ergun, R. E., Delory, G. T., Peria, W., Temerin, M., Cattell, C., et al. (1998).
762 Characteristics of electromagnetic proton cyclotron waves along auroral field lines observed by
763 FAST in regions of upward current. *Geophysical Research Letters*, 25(12), 2057–2060.
764 <https://doi.org/10.1029/98GL00513>
- 765 Chaston, C. C., Salem, C., Bonnell, J. W., Carlson, C. W., Ergun, R. E., Strangeway, R. J., &
766 McFadden, J. P. (2008). The Turbulent Alfvénic Aurora. *Physical Review Letters*, 100(17),
767 175003. <https://doi.org/10.1103/PhysRevLett.100.175003>
- 768 Clark, G., Mauk, B. H., Haggerty, D., Paranicas, C., Kollmann, P., Rymer, A., et al. (2017).
769 Energetic particle signatures of magnetic field-aligned potentials over Jupiter’s polar
770 regions. *Geophysical Research Letters*, 44(17), 8703–8711.
771 <https://doi.org/https://doi.org/10.1002/2017GL074366>
- 772 Clark, G., Mauk, B. H., Kollmann, P., Szalay, J. R., Sulaiman, A. H., Gershman, D. J., et al.
773 (2020). Energetic Proton Acceleration Associated With Io’s Footprint Tail. *Geophysical*
774 *Research Letters*, 47(24), e2020GL090839.
775 <https://doi.org/https://doi.org/10.1029/2020GL090839>
- 776 Clark, G., Tao, C., Mauk, B. H., Nichols, J., Saur, J., Bunce, E. J., et al. (2018). Precipitating
777 Electron Energy Flux and Characteristic Energies in Jupiter’s Main Auroral Region as Measured
778 by Juno/JEDI. *Journal of Geophysical Research: Space Physics*, 123(9), 7554–7567.
779 <https://doi.org/10.1029/2018JA025639>
- 780 Connerney, J. E. P., Acuña, M. H., & Ness, N. F. (1981). Modeling the Jovian current sheet and
781 inner magnetosphere. *Journal of Geophysical Research: Space Physics*, 86(A10), 8370–8384.
782 <https://doi.org/10.1029/JA086iA10p08370>
- 783 Connerney, J. E. P., Benn, M., Bjarno, J. B., Denver, T., Espley, J., Jorgensen, J. L., et al. (2017).
784 The Juno Magnetic Field Investigation. *Space Science Reviews*, 213(1), 39–138.
785 <https://doi.org/10.1007/s11214-017-0334-z>
- 786 Connerney, J. E. P., Kotsiaros, S., Oliverson, R. J., Espley, J. R., Joergensen, J. L., Joergensen, P.
787 S., et al. (2018). A New Model of Jupiter’s Magnetic Field From Juno’s First Nine
788 Orbits. *Geophysical Research Letters*, 45(6), 2590–2596. <https://doi.org/10.1002/2018GL077312>
- 789 Cowley, S. W. H., & Bunce, E. J. (2001). Origin of the main auroral oval in Jupiter’s coupled
790 magnetosphere–ionosphere system. *Planetary and Space Science*, 49(10–11), 1067–1088.
791 [https://doi.org/10.1016/S0032-0633\(00\)00167-7](https://doi.org/10.1016/S0032-0633(00)00167-7)
- 792 Delamere, P. A., & Bagenal, F. (2010). Solar wind interaction with Jupiter’s
793 magnetosphere. *Journal of Geophysical Research: Space Physics*, 115(A10).
794 <https://doi.org/10.1029/2010JA015347>
- 795 Ebert, R. W., Allegrini, F., Bagenal, F., Bolton, S. J., Connerney, J. E. P., Clark, G., et al. (2017).
796 Spatial Distribution and Properties of 0.1–100 keV Electrons in Jupiter’s Polar Auroral
797 Region. *Geophysical Research Letters*, 44(18), 9199–9207.
798 <https://doi.org/https://doi.org/10.1002/2017GL075106>

- 799 Ebert, R. W., Greathouse, T. K., Clark, G., Hue, V., Allegrini, F., Bagenal, F., et al. (n.d.).
800 Simultaneous UV Images and High-latitude Particle and Field Measurements During an Auroral
801 Dawn Storm at Jupiter. *Journal of Geophysical Research: Space Physics*, e2021JA029679.
802 <https://doi.org/10.1029/2021JA029679>
- 803 Elliott, S. S., Gurnett, D. A., Kurth, W. S., Clark, G., Mauk, B. H., Bolton, S. J., et al. (2018a).
804 Pitch Angle Scattering of Upgoing Electron Beams in Jupiter's Polar Regions by Whistler Mode
805 Waves. *Geophysical Research Letters*, 45(3), 1246–1252.
806 <https://doi.org/10.1002/2017GL076878>
- 807 Elliott, S. S., Gurnett, D. A., Kurth, W. S., Mauk, B. H., Ebert, R. W., Clark, G., et al. (2018b).
808 The Acceleration of Electrons to High Energies Over the Jovian Polar Cap via Whistler Mode
809 Wave-Particle Interactions. *Journal of Geophysical Research: Space Physics*, 123(9), 7523–
810 7533. <https://doi.org/10.1029/2018JA025797>
- 811 Elliott, S. S., Gurnett, D. A., Yoon, P. H., Kurth, W. S., Mauk, B. H., Ebert, R. W., et al. (2020).
812 The Generation of Upward-Propagating Whistler Mode Waves by Electron Beams in the Jovian
813 Polar Regions. *Journal of Geophysical Research: Space Physics*, 125(6), e2020JA027868.
814 <https://doi.org/10.1029/2020JA027868>
- 815 Elliott, S. S., Sulaiman, A. H., Kurth, W. S., Faden, J., Allegrini, F., Valek, P., et al. (2021). The
816 High-Latitude Extension of Jupiter's Io Torus: Electron Densities Measured by Juno
817 Waves. *Journal of Geophysical Research: Space Physics*, 126(8), e2021JA029195.
818 <https://doi.org/10.1029/2021JA029195>
- 819 Ergun, R. E., Andersson, L., Main, D. S., Su, Y.-J., Carlson, C. W., McFadden, J. P., & Mozer,
820 F. S. (2002). Parallel electric fields in the upward current region of the aurora: Indirect and direct
821 observations. *Physics of Plasmas*, 9(9), 3685–3694. <https://doi.org/10.1063/1.1499120>
- 822 Ergun, R. E., Carlson, C. W., McFadden, J. P., Mozer, F. S., Delory, G. T., Peria, W., et al.
823 (1998a). FAST satellite observations of electric field structures in the auroral zone. *Geophysical*
824 *Research Letters*, 25(12), 2025–2028. <https://doi.org/10.1029/98GL00635>
- 825 Ergun, R. E., Carlson, C. W., McFadden, J. P., Mozer, F. S., Delory, G. T., Peria, W., et al.
826 (1998b). FAST satellite observations of large-amplitude solitary structures. *Geophysical*
827 *Research Letters*, 25(12), 2041–2044. <https://doi.org/10.1029/98GL00636>
- 828 Farrell, W. M., Gurnett, D. A., & Goertz, C. K. (1989). Coherent Cerenkov radiation from the
829 Spacelab 2 electron beam. *Journal of Geophysical Research: Space Physics*, 94(A1), 443–452.
830 <https://doi.org/10.1029/JA094iA01p00443>
- 831 Gershman, D. J., Connerney, J. E. P., Kotsiaros, S., DiBraccio, G. A., Martos, Y. M., F. -Viñas,
832 A., et al. (2019). Alfvénic Fluctuations Associated With Jupiter's Auroral
833 Emissions. *Geophysical Research Letters*, 46(13), 7157–7165.
834 <https://doi.org/10.1029/2019GL082951>
- 835 Gladstone, G. R., Persyn, S. C., Eterno, J. S., Walther, B. C., Slater, D. C., Davis, M. W., et al.
836 (2017). The Ultraviolet Spectrograph on NASA's Juno Mission. *Space Science Reviews*, 213(1),
837 447–473. <https://doi.org/10.1007/s11214-014-0040-z>

- 838 Gladstone, G. R., Versteeg, M. H., Greathouse, T. K., Hue, V., Davis, M. W., Gérard, J.-C., et al.
839 (2017). Juno-UVS approach observations of Jupiter's auroras. *Geophysical Research*
840 *Letters*, 44(15), 7668–7675. <https://doi.org/10.1002/2017GL073377>
- 841 Gladstone, G. R., Waite, J. H., Grodent, D., Lewis, W. S., Crary, F. J., Elsner, R. F., et al. (2002).
842 A pulsating auroral X-ray hot spot on Jupiter. *Nature*, 415(6875), 1000–1003.
843 <https://doi.org/10.1038/4151000a>
- 844 Grodent, D. (2015). A Brief Review of Ultraviolet Auroral Emissions on Giant Planets. *Space*
845 *Science Reviews*, 187(1), 23–50. <https://doi.org/10.1007/s11214-014-0052-8>
- 846 Gurnett, D. A., & Shaw, R. R. (1973). Electromagnetic radiation trapped in the magnetosphere
847 above the plasma frequency. *Journal of Geophysical Research* (1896-1977), 78(34), 8136–8149.
848 <https://doi.org/10.1029/JA078i034p08136>
- 849 Gurnett, D. A. (1966). A satellite study of VLF hiss. *Journal of Geophysical Research* (1896-
850 1977), 71(23), 5599–5615. <https://doi.org/10.1029/JZ071i023p05599>
- 851 Gurnett, D. A., et al. (1983), Auroral hiss, Z mode radiation, and auroral kilometric radiation in
852 the polar magnetosphere: DE 1 observations, *Journal of Geophysical Research*, 88,
853 doi:10.1029/JA088iA01p00329
- 854 Gurnett, D. A., et al. (2011), Auroral hiss, electron beams and standing Alfvén wave currents near
855 Saturn's moon Enceladus, *Geophysical Research Letters*, 38, doi:10.1029/2011GL046854
- 856 Gurnett, D. A., Huff, R. L., Menietti, J. D., Burch, J. L., Winningham, J. D., & Shawhan, S. D.
857 (1984). Correlated low-frequency electric and magnetic noise along the auroral field
858 lines. *Journal of Geophysical Research: Space Physics*, 89(A10), 8971–8985.
859 <https://doi.org/10.1029/JA089iA10p08971>
- 860 Hill, T. W. (2001). The Jovian auroral oval. *Journal of Geophysical Research: Space*
861 *Physics*, 106(A5), 8101–8107. <https://doi.org/10.1029/2000JA000302>
- 862 Hill, T. W. (1979). Inertial limit on corotation. *Journal of Geophysical Research: Space*
863 *Physics*, 84(A11), 6554–6558. <https://doi.org/10.1029/JA084iA11p06554>
- 864 Hull, A. J., Bonnell, J. W., Mozer, F. S., & Scudder, J. D. (2003). A statistical study of large-
865 amplitude parallel electric fields in the upward current region of the auroral acceleration
866 region. *Journal of Geophysical Research: Space Physics*, 108(A1), SMP 5-1-SMP 5-23.
867 <https://doi.org/10.1029/2001JA007540>
- 868 Imai, M., Greathouse, T. K., Kurth, W. S., Gladstone, G. R., Louis, C. K., Zarka, P., et al.
869 (2019). Probing Jovian Broadband Kilometric Radio Sources Tied to the Ultraviolet Main
870 Auroral Oval With Juno. *Geophysical Research Letters*, 46(2), 571–579.
871 <https://doi.org/10.1029/2018GL081227>
- 872 James, H. G. VLF saucers, *J. Geophys. Res.*, **81**, 4 (1976). doi:10.1029/JA081i004p00501

- 873 Joy, S. P., Kivelson, M. G., Walker, R. J., Khurana, K. K., Russell, C. T., & Ogino, T. (2002).
874 Probabilistic models of the Jovian magnetopause and bow shock locations. *Journal of*
875 *Geophysical Research: Space Physics*, 107(A10), SMP 17-1-SMP 17-17.
876 <https://doi.org/https://doi.org/10.1029/2001JA009146>
- 877 Khurana, K. K., Kivelson, M. G., Vasylunas, V. M., Krupp, N., Woch, J., Lagg, A., et al.
878 (2004). The configuration of Jupiter's magnetosphere. In F. Bagenal, T. E. Dowling, & W. B.
879 McKinnon (Eds.), *Jupiter: The planet, satellites, and magnetosphere* (pp. 593-616). New York.
880 Cambridge Uni. Press.
- 881 Kivelson, M. G., & Southwood, D. J. (2005). Dynamical consequences of two modes of
882 centrifugal instability in Jupiter's outer magnetosphere. *Journal of Geophysical Research: Space*
883 *Physics*, 110(A12). <https://doi.org/10.1029/2005JA011176>
- 884 Knight, S. (1973). Parallel electric fields. *Planetary and Space Science*, 21(5), 741–750.
885 [https://doi.org/10.1016/0032-0633\(73\)90093-7](https://doi.org/10.1016/0032-0633(73)90093-7)
- 886 Kolmašová, I., Imai, M., Santolík, O., Kurth, W. S., Hospodarsky, G. B., Gurnett, D. A., et al.
887 (2018). Discovery of rapid whistlers close to Jupiter implying lightning rates similar to those on
888 Earth. *Nature Astronomy*, 2(7), 544–548. <https://doi.org/10.1038/s41550-018-0442-z>
- 889 Kotsiaros, S., Connerney, J. E. P., Clark, G., Allegrini, F., Gladstone, G. R., Kurth, W. S., et al.
890 (2019). Birkeland currents in Jupiter's magnetosphere observed by the polar-orbiting Juno
891 spacecraft. *Nature Astronomy*, 3(10), 904–909. <https://doi.org/10.1038/s41550-019-0819-7>
- 892 Kurth, W. S., Hospodarsky, G. B., Kirchner, D. L., Mokrzycki, B. T., Averkamp, T. F., Robison,
893 W. T., et al. (2017b). The Juno Waves Investigation. *Space Science Reviews*, 213(1), 347–392.
894 <https://doi.org/10.1007/s11214-017-0396-y>
- 895 Kurth, W. S., Imai, M., Hospodarsky, G. B., Gurnett, D. A., Louarn, P., Valek, P., et al. (2017a).
896 A new view of Jupiter's auroral radio spectrum. *Geophysical Research Letters*, 44(14), 7114–
897 7121. <https://doi.org/10.1002/2017GL072889>
- 898 Kurth, W. S., Mauk, B. H., Elliott, S. S., Gurnett, D. A., Hospodarsky, G. B., Santolík, O., et al.
899 (2018). Whistler Mode Waves Associated With Broadband Auroral Electron Precipitation at
900 Jupiter. *Geophysical Research Letters*, 45(18), 9372–9379.
901 <https://doi.org/10.1029/2018GL078566>
- 902 Li, W., Thorne, R. M., Ma, Q., Zhang, X.-J., Gladstone, G. R., Hue, V., et al. (2017).
903 Understanding the Origin of Jupiter's Diffuse Aurora Using Juno's First Perijove
904 Observations. *Geophysical Research Letters*, 44(20), 10,162-10,170.
905 <https://doi.org/10.1002/2017GL075545>
- 906 Li, W., Ma, Q., Shen, X.-C., Zhang, X.-J., Mauk, B. H., Clark, G., et al. (2021). Quantification of
907 Diffuse Auroral Electron Precipitation Driven by Whistler Mode Waves at Jupiter. *Geophysical*
908 *Research Letters*, 48(19), e2021GL095457. <https://doi.org/10.1029/2021GL095457>
- 909 Louarn, P., Allegrini, F., McComas, D. J., Valek, P. W., Kurth, W. S., André, N., et al. (2017).
910 Generation of the Jovian hectometric radiation: First lessons from Juno: Juno Observations in a

- 911 HOM Radio Source. *Geophysical Research Letters*, 44(10), 4439–4446.
912 <https://doi.org/10.1002/2017GL072923>
- 913 Louis, C. K., Prangé, R., Lamy, L., Zarka, P., Imai, M., Kurth, W. S., & Connerney, J. E. P.
914 (2019). Jovian Auroral Radio Sources Detected In Situ by Juno/Waves: Comparisons With
915 Model Auroral Ovals and Simultaneous HST FUV Images. *Geophysical Research*
916 *Letters*, 46(21), 11606–11614. <https://doi.org/10.1029/2019GL084799>
- 917 Lysak, R. L. (1986). Ion Acceleration by Wave-Particle Interaction. In *Ion Acceleration in the*
918 *Magnetosphere and Ionosphere* (pp. 261–270). American Geophysical Union (AGU).
919 <https://doi.org/10.1029/GM038p0261>
- 920 Lysak, R. L. (1991). Feedback instability of the ionospheric resonant cavity. *Journal of*
921 *Geophysical Research: Space Physics*, 96(A2), 1553–1568. <https://doi.org/10.1029/90JA02154>
- 922 Lysak, R. L., Song, Y., Elliott, S., Kurth, W., Sulaiman, A. H., & Gershman, D. (2021). The Jovian
923 Ionospheric Alfvén Resonator and Auroral Particle Acceleration. *Journal of Geophysical*
924 *Research: Space Physics*, e2021JA029886. <https://doi.org/10.1029/2021JA029886>
- 925 Maggs, J. E., et al. (1989), Nonlinear evolution of the auroral electron beam, *Journal of*
926 *Geophysical Research*, 94, doi:10.1029/JA094iA04p03631
- 927 Masters, A. (2017). Model-Based Assessments of Magnetic Reconnection and Kelvin-Helmholtz
928 Instability at Jupiter’s Magnetopause. *Journal of Geophysical Research: Space Physics*, 122(11),
929 11,154–11,174. <https://doi.org/10.1002/2017JA024736>
- 930 Masters, A. (2018). A More Viscous-Like Solar Wind Interaction With All the Giant
931 Planets. *Geophysical Research Letters*, 45(15), 7320–7329.
932 <https://doi.org/10.1029/2018GL078416>
- 933 Masters, A., Dunn, W. R., Stallard, T. S., Manners, H., & Stawarz, J. (2021). Magnetic
934 Reconnection Near the Planet as a Possible Driver of Jupiter’s Mysterious Polar
935 Auroras. *Journal of Geophysical Research: Space Physics*, 126(8), e2021JA029544.
936 <https://doi.org/10.1029/2021JA029544>
- 937 Matsumoto, H., Kojima, H., Miyatake, T., Omura, Y., Okada, M., Nagano, I., & Tsutsui, M.
938 (1994). Electrostatic solitary waves (ESW) in the magnetotail: BEN wave forms observed by
939 GEOTAIL. *Geophysical Research Letters*, 21(25), 2915–2918.
940 <https://doi.org/10.1029/94GL01284>
- 941 Mauk, B. H., Clark, G., Gladstone, G. R., Kotsiaros, S., Adriani, A., Allegrini, F., et al. (2020).
942 Energetic Particles and Acceleration Regions Over Jupiter’s Polar Cap and Main Aurora: A
943 Broad Overview. *Journal of Geophysical Research: Space Physics*, 125(3), e2019JA027699.
944 <https://doi.org/https://doi.org/10.1029/2019JA027699>
- 945 Mauk, B. H., Haggerty, D. K., Paranicas, C., Clark, G., Kollmann, P., Rymer, A. M., et al.
946 (2017a). Juno observations of energetic charged particles over Jupiter’s polar regions: Analysis
947 of monodirectional and bidirectional electron beams. *Geophysical Research Letters*, 44(10),
948 4410–4418. <https://doi.org/10.1002/2016GL072286>

- 949 Mauk, B. H., Haggerty, D. K., Paranicas, C., Clark, G., Kollmann, P., Rymer, A. M., et al.
950 (2017b). Discrete and broadband electron acceleration in Jupiter's powerful
951 aurora. *Nature*, 549(7670), 66–69. <https://doi.org/10.1038/nature23648>
- 952 Mauk, B. H., Haggerty, D. K., Jaskulek, S. E., Schlemm, C. E., Brown, L. E., Cooper, S. A., et
953 al. (2017c). The Jupiter Energetic Particle Detector Instrument (JEDI) Investigation for the Juno
954 Mission. *Space Science Reviews*, 213(1), 289–346. <https://doi.org/10.1007/s11214-013-0025-3>
- 955 Mauk, B. H., Haggerty, D. K., Paranicas, C., Clark, G., Kollmann, P., Rymer, A. M., et al.
956 (2018). Diverse Electron and Ion Acceleration Characteristics Observed Over Jupiter's Main
957 Aurora. *Geophysical Research Letters*, 45(3), 1277–1285.
958 <https://doi.org/10.1002/2017GL076901>
- 959 McComas, D. J., Alexander, N., Allegrini, F., Bagenal, F., Beebe, C., Clark, G., et al. (2017).
960 The Jovian Auroral Distributions Experiment (JADE) on the Juno Mission to Jupiter. *Space*
961 *Science Reviews*, 213(1), 547–643. <https://doi.org/10.1007/s11214-013-9990-9>
- 962 McComas, D. J., & Bagenal, F. (2007). Jupiter: A fundamentally different magnetospheric
963 interaction with the solar wind. *Geophysical Research Letters*, 34(20), 421–5.
964 <http://doi.org/10.1029/2007GL031078>
- 965 McFadden, J. P., Carlson, C. W., Ergun, R. E., Chaston, C. C., Mozer, F. S., Temerin, M., et al.
966 (1998). Electron modulation and ion cyclotron waves observed by FAST. *Geophysical Research*
967 *Letters*, 25(12), 2045–2048. <https://doi.org/10.1029/98GL00855>
- 968 McIlwain, C. E. (1961), Coordinates for mapping the distribution of magnetically trapped
969 particles, *Journal of Geophysical Research*, 66, doi:10.1029/JZ066i011p03681
- 970 Mitchell, D. G., Kurth, W. S., Hospodarsky, G. B., Krupp, N., Saur, J., Mauk, B. H., et al.
971 (2009). Ion conics and electron beams associated with auroral processes on Saturn. *Journal of*
972 *Geophysical Research: Space Physics*, 114(A2). <https://doi.org/10.1029/2008JA013621>
- 973 Mura, A., Adriani, A., Altieri, F., Connerney, J. E. P., Bolton, S. J., Moriconi, M. L., et al.
974 (2017). Infrared observations of Jovian aurora from Juno's first orbits: Main oval and satellite
975 footprints. *Geophysical Research Letters*, 44(11), 5308–5316.
976 <https://doi.org/10.1002/2017GL072954>
- 977 Nichols, J. D., & Cowley, S. W. H. (2004). Magnetosphere-ionosphere coupling currents in
978 Jupiter's middle magnetosphere: effect of precipitation-induced enhancement of the ionospheric
979 Pedersen conductivity. *Annales Geophysicae*, 22(5), 1799–1827.
980 <https://doi.org/https://doi.org/10.5194/angeo-22-1799-2004>
- 981 Paranicas, C., Mauk, B. H., Haggerty, D. K., Clark, G., Kollmann, P., Rymer, A. M., et al.
982 (2018). Intervals of Intense Energetic Electron Beams Over Jupiter's Poles. *Journal of*
983 *Geophysical Research: Space Physics*, 123(3), 1989–1999.
984 <https://doi.org/https://doi.org/10.1002/2017JA025106>

- 985 Paschmann, G., Haaland, S., & Treumann, R. (2003). The Aurora as a Universal Phenomenon. In
986 G. Paschmann, S. Haaland, & R. Treumann (Eds.), *Auroral Plasma Physics* (pp. 415–434).
987 Dordrecht: Springer Netherlands. https://doi.org/10.1007/978-94-007-1086-3_9
- 988 Persoon, A. M., Gurnett, D. A., Peterson, W. K., Waite Jr., J. H., Burch, J. L., & Green, J. L.
989 (1988). Electron density depletions in the nightside auroral zone. *Journal of Geophysical*
990 *Research: Space Physics*, 93(A3), 1871–1895. <https://doi.org/10.1029/JA093iA03p01871>
- 991 Persoon, A. M., Kurth, W. S., Gurnett, D. A., Groene, J. B., Sulaiman, A. H., Wahlund, J.-E., et
992 al. (2019). Electron Density Distributions in Saturn’s Ionosphere. *Geophysical Research*
993 *Letters*, 46(6), 3061–3068. <https://doi.org/10.1029/2018GL078020>
- 994 Ray, L. C., Ergun, R. E., Delamere, P. A., & Bagenal, F. (2010). Magnetosphere-ionosphere
995 coupling at Jupiter: Effect of field-aligned potentials on angular momentum transport. *Journal of*
996 *Geophysical Research: Space Physics*, 115(A9).
997 <https://doi.org/https://doi.org/10.1029/2010JA015423>
- 998 Ray, L. C., Su, Y.-J., Ergun, R. E., Delamere, P. A., & Bagenal, F. (2009). Current-voltage
999 relation of a centrifugally confined plasma. *Journal of Geophysical Research: Space*
1000 *Physics*, 114(A4). <https://doi.org/10.1029/2008JA013969>
- 1001 Santolík, O., & Gurnett, D. A. (2002). Propagation of auroral hiss at high altitudes: Propagation
1002 of auroral hiss at high altitudes. *Geophysical Research Letters*, 29(10), 119-1-119-4.
1003 <https://doi.org/10.1029/2001GL013666>
- 1004 Santolík, O., et al. (2016), Propagation of equatorial noise to low altitudes: Decoupling from the
1005 magnetosonic mode, *Geophysical Research Letters*, 43, 13, doi:10.1002/2016GL069582
- 1006 Saur, J., Janser, S., Schreiner, A., Clark, G., Mauk, B. H., Kollmann, P., et al. (2018). Wave-
1007 Particle Interaction of Alfvén Waves in Jupiter’s Magnetosphere: Auroral and Magnetospheric
1008 Particle Acceleration. *Journal of Geophysical Research: Space Physics*, 123(11), 9560–9573.
1009 <https://doi.org/https://doi.org/10.1029/2018JA025948>
- 1010 Saur, J., Politano, H., Pouquet, A., & Matthaeus, W. H. (2002). Evidence for weak MHD
1011 turbulence in the middle magnetosphere of Jupiter. *Astronomy & Astrophysics*, 386(2), 699–708.
1012 <https://doi.org/10.1051/0004-6361:20020305>
- 1013 Saur, J., Pouquet, A., & Matthaeus, W. H. (2003). An acceleration mechanism for the generation
1014 of the main auroral oval on Jupiter. *Geophysical Research Letters*, 30(5).
1015 <https://doi.org/https://doi.org/10.1029/2002GL015761>
- 1016 Shi, C., Zhao, J., Sun, H., Huang, C., & Xie, H. (2020). Electromagnetic Emission Driven by
1017 Electron Beam Instability in the Jovian Polar Regions. *The Astrophysical Journal*, 902(2), 151.
1018 <https://doi.org/10.3847/1538-4357/abb5a1>
- 1019 Song, Y., & Lysak, R. L. (2006). Displacement Current and the Generation of Parallel Electric
1020 Fields. *Physical Review Letters*, 96(14), 145002. <https://doi.org/10.1103/PhysRevLett.96.145002>
- 1021 Sulaiman, A. H. et al. (2018), Enceladus auroral hiss emissions during Cassini’s Grand Finale,
1022 *Geophys. Res. Lett.*, **45**, 15, doi:10.1029/2018GL078130

- 1023 Sulaiman, A. H., Elliott, S. S., Kurth, W. S., Faden, J. B., Hospodarsky, G. B., & Menietti, J. D.
1024 (2021). Inferring Jovian Electron Densities Using Plasma Wave Spectra Obtained by the
1025 Juno/Waves Instrument. *Journal of Geophysical Research: Space Physics*, 126(8),
1026 e2021JA029263. <https://doi.org/10.1029/2021JA029263>
- 1027 Sulaiman, A. H., Hospodarsky, G. B., Elliott, S. S., Kurth, W. S., Gurnett, D. A., Imai, M., et al.
1028 (2020). Wave-Particle Interactions Associated With Io's Auroral Footprint: Evidence of Alfvén,
1029 Ion Cyclotron, and Whistler Modes. *Geophysical Research Letters*, 47(22), e2020GL088432.
1030 <https://doi.org/10.1029/2020GL088432>
- 1031 Szalay, J. R., Allegrini, F., Bagenal, F., Bolton, S. J., Clark, G., Connerney, J. E. P., et al. (2017).
1032 Plasma measurements in the Jovian polar region with Juno/JADE. *Geophysical Research Letters*,
1033 86(A8), 8447–9. <http://doi.org/10.1002/2017GL072837>
- 1034 Szalay, J. R., Allegrini, F., Bagenal, F., Bolton, S. J., Clark, G., Connerney, J. E. P., et al. (2021).
1035 Proton Outflow Associated With Jupiter's Auroral Processes. *Geophysical Research*
1036 *Letters*, 48(1). <https://doi.org/10.1029/2020GL091627>
- 1037 Temerin, M., Cerny, K., Lotko, W., & Mozer, F. S. (1982). Observations of Double Layers and
1038 Solitary Waves in the Auroral Plasma. *Physical Review Letters*, 48(17), 1175–1179.
1039 <https://doi.org/10.1103/PhysRevLett.48.1175>
- 1040 Thomas, N., Bagenal, F., Hill, T. W., & Wilson, J. K. (2004). The Io neutral clouds and plasma
1041 torus. In F. Bagenal, T. E. Dowling, & W. B. McKinnon (Eds.), *Jupiter: The planet, satellites,*
1042 *and magnetosphere* (pp. 593-616). New York. Cambridge Uni. Press.
- 1043 Waite, J. H., Gladstone, G. R., Lewis, W. S., Goldstein, R., McComas, D. J., Riley, P., et al.
1044 (2001). An auroral flare at Jupiter. *Nature*, 410(6830), 787–789.
1045 <https://doi.org/10.1038/35071018>
- 1046 Wu, C. S., & Lee, L. C. (1979). A theory of the terrestrial kilometric radiation. *The Astrophysical*
1047 *Journal*, 230, 621-626. <https://doi.org/10.1086/157120>
- 1048 Zhang, B., Delamere, P. A., Yao, Z., Bonfond, B., Lin, D., Sorathia, K. A., et al. (n.d.). How
1049 Jupiter's unusual magnetospheric topology structures its aurora. *Science Advances*, 7(15),
1050 eabd1204. <https://doi.org/10.1126/sciadv.abd1204>
- 1051
- 1052
- 1053
- 1054
- 1055